Open Access

Earth System
Science
Data

Reconstructed global monthly burned area maps from 1901 to 2020

Zhixuan Guo[1], Wei Li[1], Philippe Ciais[2], Stephen Sitch[3], Guido R. van der Werf[4], Simon P. K. Bowring[2], Ana Bastos[5], Florent Mouillot[6], Jiaying He[7], Minxuan Sun[1], Lei Zhu[1], Xiaomeng Du[1], Nan Wang[1], and Xiaomeng Huang[1]

[1]Department of Earth System Science, Ministry of Education Key Laboratory for Earth System Modeling, Institute for Global Change Studies, Tsinghua University, Beijing 100084, China
[2]Laboratoire des Sciences du Climat et de l'Environnement, LSCE/IPSL, CEA-CNRS-UVSQ, Université Paris-Saclay, 91191 Gif-sur-Yvette, France
[3]Faculty of Environment, Science and Economy, University of Exeter, Exeter, EX4 4QF, UK
[4]Environmental Sciences Group, Wageningen University, P.O. Box 47, 6700AA, Wageningen, the Netherlands
[5]Institute for Earth System Science and Remote Sensing, Leipzig University, Talstr. 35, 04103 Leipzig, Germany
[6]UMR CEFE 5175, Univ Montpellier, CNRS, EPHE, IRD, 1919 Route de Mende, CEDEX 5, 34293 Montpellier, France
[7]State Key Laboratory of Resources and Environmental Information System, Institute of Geographic Sciences and Natural Resources Research, Chinese Academy of Sciences, Beijing 100101, China

Correspondence: Wei Li (wli2019@tsinghua.edu.cn)

Abstract. Fire is a key Earth system process, driving variability in the global carbon cycle through CO_2 emissions into the atmosphere and subsequent CO_2 uptake through vegetation recovery after fires. Global spatiotemporally consistent datasets on burned area have been available since the beginning of the satellite era in the 1980s, but they are sparse prior to that date. In this study, we reconstructed global monthly burned area at a resolution of $0.5° \times 0.5°$ from 1901 to 2020 using machine learning models trained on satellite-based observations of burned area between 2003 and 2020, with the goal of reconstructing long-term burned area information to constrain historical fire simulations. We first conducted a classification model to separate grid cells with extreme (burned area $\geq$ the 90th percentile in a given region) or regular fires. We then trained separate regression models for grid cells with extreme or regular fires. Both the classification and regression models were trained on a satellite-based burned area product (FireCCI51), using explanatory variables related to climate, vegetation and human activities. The trained models can well reproduce the long-term spatial patterns (slopes $= 0.70$–1.28 and $R^2 = 0.69$–0.98 spatially), inter-annual variability and seasonality of the satellite-based burned area observations. After applying the trained model to the historical period, the predicted annual global total burned area ranges from 3.46×10^6 to 4.58×10^6 km^2 yr^{-1} over 1901–2020 with regular and extreme fires accounting for 1.36×10^6–1.74×10^6 and 2.00×10^6–3.03×10^6 km^2 yr^{-1}, respectively. Our models estimate a global decrease in burned area during 1901–1978 (slope $= -0.009 \times 10^6$ km^2 yr^{-2}), followed by an increase during 1978–2008 (slope $= 0.020 \times 10^6$ km^2 yr^{-2}), and then a stronger decline in 2008–2020 (slope $= -0.049 \times 10^6$ km^2 yr^{-2}). Africa was the continent with the largest burned area globally during 1901–2020, and its trends also dominated the global trends. We validated our predictions against charcoal records, and our product exhibits a high overall accuracy in simulating fire occurrence ($> 80\%$) in boreal North America, southern Europe, South America, Africa and southeast Australia, but the overall accuracy is relatively lower in northern Europe and Asia ($< 50\%$). In addition, we compared our burned area data with multiple independent regional burned

area maps in Canada, the USA, Brazil, Chile and Europe, and found general consistency in the spatial patterns (linear regression slopes ranging 0.84–1.38 spatially) and the inter-annual variability. The global monthly $0.5° \times 0.5°$ burned area fraction maps for 1901–2020 presented by this study can be downloaded for free from https://doi.org/10.5281/zenodo.14191467 (Guo and Li, 2024).

1   Introduction

Fire is an important component of the Earth system (Bowman et al., 2009; Bowman et al., 2020), having large impacts on ecosystems by altering vegetation structure and function (Bond et al., 2005; Lasslop et al., 2016), and affecting the regional or even global energy budget through changes in surface albedo (Randerson et al., 2006) and aerosol and greenhouse gas emissions (van der Werf et al., 2010). Vegetation recovery after fires also contributes to a legacy carbon flux into the ecosystem carbon sink (Hudiburg et al., 2023; Song et al., 2018; Yue et al., 2020). In contrast, fire occurrence and spread are controlled by complex factors such as climatic conditions, vegetation states, ignition foci, anthropogenic activities and their interactions (Andela et al., 2017; Flannigan et al., 2009; Jones et al., 2022; Senande-Rivera et al., 2022). Therefore, accurately mapping spatiotemporal patterns in global burned area is essential for understanding the mechanisms of fire disturbances and quantifying the global carbon budget and local energy balance (Mouillot et al., 2014).

Satellites provide direct observations of fire activities (e.g., burned area and fire radiative power) (Andela et al., 2017; Giglio et al., 2006; Luo et al., 2024), but they have limited temporal coverage because most satellite data are available for only after the 1980s (Chuvieco et al., 2019). Fire modules in dynamic global vegetation models (DGVMs) are able to simulate long-term burned area and interactions with vegetation dynamics based on climate conditions and soil properties (Sitch et al., 2015, 2024), but the spatial resolution at the global scale is usually coarse due to the coarse resolution of the input meteorological forcing data, and most models fail to capture global trends in burned area (Andela et al., 2017; Hantson et al., 2020). The processes included and the parameterizations of fire processes vary widely across fire models, resulting in a large range of simulated burned area at both the regional and global scales (Hantson et al., 2020). Considering the limitations of satellite observations and fire models, spatiotemporally consistent burned area maps for the 20th century, trained on present-day observations, are essential for fire modeling and can serve as publicly available benchmarks for fire ecology and carbon cycle studies.

A previous study synthesized historical statistics on burned area and a reconstructed global fire history of the 20th century at the decadal scale using statistical models and a prescribed fire probability map from satellites (Mouillot and Field, 2005). This dataset is valuable since it incorporates many historical national fire records, despite being prone to uncertainties. Machine learning models are now widespread and constitute appropriate tools to capture non-linearity in complex systems such as wildfires and have been used to predict burned area based on climate, fuel conditions and anthropogenic activities, but the temporal coverage of predictions is sometimes limited by the input data (Jain et al., 2020; Joshi and Sukumar, 2021; Li et al., 2023). There have been attempts to integrate machine learning models to replace process-based wildfire models in Earth system models. Machine learning models also exhibit better performance than process-based wildfire models even though they heavily depend on the input data that are simulated – often with substantial uncertainty – by Earth system models (Zhu et al., 2022). It is challenging for machine learning models to predict extreme values, because extreme values are often treated as outliers and are limited by the sample size (Breunig et al., 2000; Ribeiro and Moniz, 2020). However, extreme fires, usually defined as fires with an unprecedented scale or intensity (Bowman et al., 2017; Castro Rego et al., 2021; Cunningham et al., 2024), have significantly greater impacts than regular fires as they release more CO_2, altering hydrological cycles and emitting higher levels of pollutants (Clarke et al., 2022; Page et al., 2011).

In this study, we produced a global monthly $0.5° \times 0.5°$ burned area fraction (BAF) dataset for 1901–2020 (Guo and Li, 2024) using machine learning models based on climate conditions, vegetation states, population density and land use data (Table 1). To better capture extreme fires, we developed a classification model to distinguish grid cells with extreme or regular fires. To define extreme fires, we used the 90th percentile of burned area fractions within a region as the threshold. We then trained separate regression models on grid cells categorized as having extreme or regular fires. The models were trained against the satellite-based burned area product (FireCCI51) for 2003–2020. We then used the models to reconstruct the burned area from 1901 to 2020. In addition to evaluating the models against satellite observations that were not used for model training, we also compared our burned area predictions with charcoal records and other independent global and regional burned area datasets (Table 2).

2   Methods

The workflow of this study is illustrated in Fig. 1. The datasets used for extracting predictors and comparisons are listed in Tables 1 and 2, respectively. We first divided the

globe into 14 regions (Fig. S1 in the Supplement) following the Global Fire Emission Dataset (GFED regions) (Giglio et al., 2006; van der Werf et al., 2017) and conducted machine learning model training, testing and prediction in each GFED region individually. The 14 GFED regions were abbreviated as BONA (Boreal North America), TENA (Temperate North America), CEAM (Central America), NHSA (Northern Hemisphere South America), SHSA (Southern Hemisphere South America), EURO (Europe), MIDE (Middle East), NHAF (Northern Hemisphere Africa), SHAF (Southern Hemisphere Africa), BOAS (Boreal Asia), CEAS (Central Asia), SEAS (Southeast Asia), EQAS (Equatorial Asia) and AUST (Australia and Aotearoa / New Zealand).

2.1 Data preparation

We used data from the satellite-based monthly global burned area grid product FireCCI51 (2003–2020) (Lizundia-Loiola et al., 2020) for model training. This dataset was resampled from the original resolution, $0.25° × 0.25°$, to $0.5° × 0.5°$. We excluded all burned pixels overlapping cropland classes in the CCI land-cover layer provided with FireCCI51 (Lizundia-Loiola et al., 2020) to remove agricultural fires from our analysis. We used the 90th percentile of burned area fractions across the $0.5° × 0.5°$ grid cells within a region as the threshold for defining extreme fires. This percentile was chosen based on the previous literature (Bowman et al., 2017; Cunningham et al., 2024; Lannom et al., 2014). It is high enough ($\geq$ 90th) to distinguish moderate from extreme samples to train separate models for each category. Meanwhile, it is not too high (e.g., 95th or 99th) in regions with limited data (such as Europe and the Middle East), ensuring sufficient extreme samples for model training and evaluation. The monthly distribution of burned area within the $0.5° × 0.5°$ grid cells (Fig. S2) shows that if regular and extreme fires are modeled together (black curves), the abundant moderate values drown out the extremes (orange curves), causing the total burned area to be underestimated. We thus first conducted a classification and then trained separate models for regular and extreme burned fractions to enhance the representation of extreme events and improve regression performance. We used 16 explanatory variables to represent climate, vegetation and anthropogenic effects on regular and extreme BAF in machine learning models (Table 1).

Climatic variables, including the daily maximum temperature (Tmax), daily minimum temperature (Tmin), precipitation (Precip) and wind speed (Wind) were directly extracted and resampled to a monthly time step from CRUJRA v2.2, a global climate forcing dataset covering the period 1901–2020 with a 6-hourly temporal resolution and a $0.5° × 0.5°$ spatial resolution (Harris et al., 2014, 2020; Kobayashi et al., 2015). Vapor pressure deficit (VPD) was calculated using empirical equations (Buck, 1981) based on air temperature, air pressure and specific humidity data from CRUJRA v2.2 at the 6 h step and then averaged to the monthly scale. The fire

weather index (FWI), a numeric rating of fire intensity used in the Canadian Forest Fire Weather Index System (Wagner, 1987), was calculated using the "cffdrs" package (Wang et al., 2017) in R programming language (R Core Team, 2024). Air temperature, relative humidity, wind speed and precipitation were derived from CRUJRA v2.2 at the daily time step, which was then averaged to monthly.

Variables related to anthropogenic effects include population density, land use and land use change fractions. Population density was resampled to the $0.5° × 0.5°$ scale from HYDE3.2, a global population density dataset with a spatial resolution of 5 arcmin available from 10 000 BCE to 2015 CE (Klein Goldewijk et al., 2017). Land use fractions refer to the area fraction of a certain land use type in each $0.5° × 0.5°$ grid cell in the current year, and land use change fractions are the difference in land use fractions between the current year and the previous year. We use the area fractions of four land use types (forest, shrub, natural grass and cropland) from the ESA CCI land cover maps for 1992–2020 (Li et al., 2018), and the Land Use Harmonization 2 dataset for the Global Carbon Budget 2020 (LUH2-GCB2020) for the period before 1992 (Chini et al., 2021), following the methods used by Peng et al. (2017). In the land use harmonization process, we resampled both ESA CCI and LUH2 datasets to $0.5° × 0.5°$ and reclassified them into five land use types (forest, shrub, natural grass, cropland and others). The above five land use types were converted from the ESA CCI land-cover maps based on a cross-walking table (Li et al., 2018). For the LUH2 dataset, we reclassified land use by summing forested primary land (primf) and potentially forested secondary land (secdf), to create a single "forest" category, and by summing all crop types (c3ann, c3per, c3nfx, c4ann, and c4per) to form the "cropland" category. To define natural grass and shrub, we first combined non-forested primary land (primn) and potentially non-forested secondary land (secdn) into a unified grass + shrub type. We then allocated this combined area to separate grass and shrub categories based on their proportional distribution. For the period before 1992, the proportional distribution was set the same as ESA CCI land cover in 1992, and for years in the period 1992–2020, the proportional distribution was set according to the corresponding year of ESA CCI land cover. The area fraction changes between two consecutive years in LUH2 were used to extrapolate the land use fraction in each year before 1992. Therefore, the harmonized land use maps adopted the inter-annual variability from LUH2-GCB2020 before 1992, while the absolute area fractions were based on the ESA CCI maps. Comparisons of LUH2-GCB2020, ESA CCI maps and the harmonized maps in this study are shown in Fig. S3. Among the five land use types, four of them (forest, shrub, natural grass and cropland) were used as input to the machine learning models.

We used the leaf area index (LAI) in the previous three months as a proxy for fuel status for the fire activity in the current month. Global monthly LAI maps in $0.5° × 0.5°$ grid cells are resampled from GIMMS LAI4g, a satellite-based
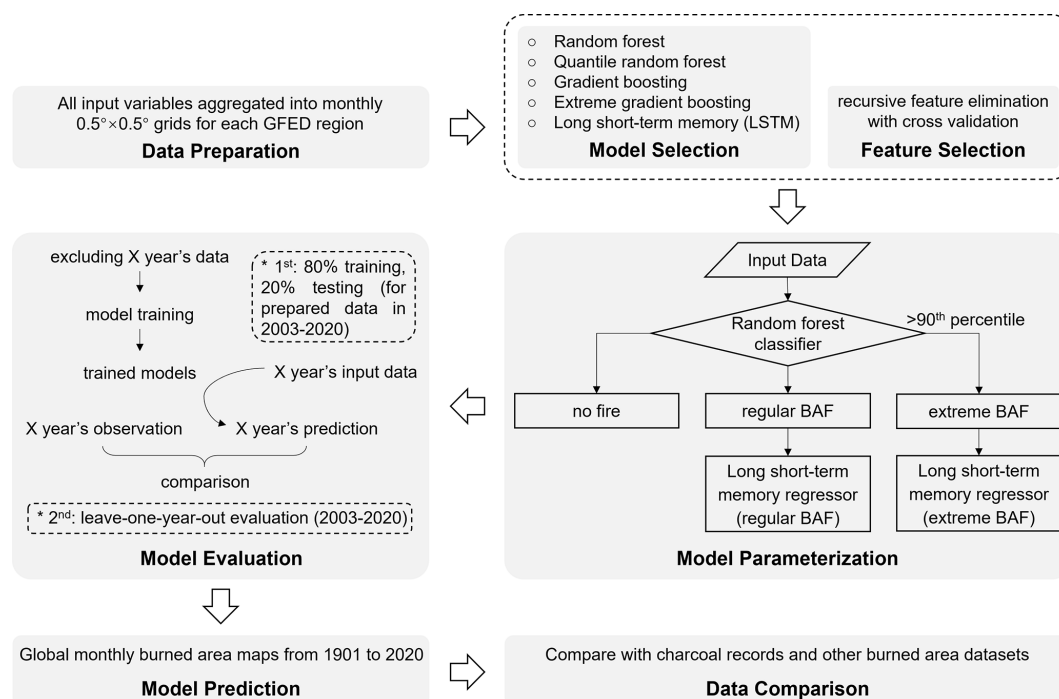
Figure 1. Workflow of this study.

global LAI dataset available every half-month for 1982–2020 with a spatial resolution of 5 arcmin (Cao et al., 2023). After bias corrections, we further generated LAI data for 1901–1981 using the multi-model average LAI from S3 simulations incorporating dynamic climate, CO_2 and land use change by eight DGVMs (EDv3, IBIS, ISAM, LPJ-GUESS, LPJmL, LPX-Bern, ORCHIDEE, and VISIT) in TRENDY v11 (Sitch et al., 2024). In the bias correction process, maps indicating the global monthly LAI difference (defined as LAI bias) between the GIMMS LAI4g dataset and multi-model averages from TRENDY v11 were firstly calculated for 1982–2020, and then machine learning models were utilized to predict the LAI biases for 1901–1981 using 15 variables (the variables in Table 1 excluding LAI and BAF) after model training and testing with data covering 1982–2020 (80 % for training and 20 % for testing) in each region. Finally, the harmonized LAI during 1901–1981 is equal to the sum of the multi-model average LAI from TRENDY v11 and the predicted LAI biases. The LAI for 1982–2020 was directly derived from GIMMS LAI4g. The harmonized LAI maps therefore adopt the inter-annual and inter-monthly variability of TRENDY v11 to extrapolate the temporal coverage of GIMMS LAI4g to before 1982. Comparisons of the LAI from GIMMS LAI4g, TRENDY v11 and the harmonized data in this study are shown in Figs. S4–S6.

All datasets were aggregated into monthly data with a spatial resolution of $0.5° × 0.5°$ for the training and prediction of the machine learning models.

2.2 Machine learning models

For each region (Fig. S1), we fed BAF as the dependent variable, and the 16 explanatory variables (Table 1) as independent variables to build the machine learning models individually. To better capture extreme fires, we first developed a random forest classification model to distinguish grid cells ($0.5° × 0.5°$) with no BAF, regular BAF or extreme BAF. Extreme fire is usually defined by a percentile threshold of fire size, fire radiative power or the fire spread rate in a region (Bowman et al., 2017; Castro Rego et al., 2021; Cunningham et al., 2024). Here, we defined grid cells with extreme BAF as grid cells with a BAF exceeding the 90th percentile of all grid cells with fires in each region through the entire period (2003–2020). Other grid cells with a BAF greater than 0 were thus treated as grid cells with a regular BAF. To balance sample sizes across BAF types, we applied a weighting method in the machine learning classification models. Let the sample counts for no BAF, regular BAF and extreme BAF be n1, n2 and n3, respectively. We computed their least common multiple, M, and assigned weights of M/n1, M/n2 and M/n3 to each BAF type. After classification, we performed machine learning regressions separately for grid cells with a regular or extreme BAF. Grid cells for each category (regular and extreme) were fed into separate regression models to estimate the specific BAF value (continuous values).

For the regression model selection, we tested commonly used machine learning models, including random forest (Tin Kam, 1995), quantile random forest (Meinshausen, 2006),

Table 1. Explanatory variables used in the machine learning models.

Variables	Descriptions	Datasets	References
Tmax	Daily maximum temperature (°C)	CRU JRA v2.2	Harris et al. (2014, 2020); Kobayashi et al. (2015)
Tmin	Daily minimum temperature (°C)		
Precip	Monthly total precipitation (mm/month)		
Wind	Wind speed ($m\,s^{-1}$)		
VPD	Vapor pressure deficit (hPa)	Calculated based on CRU JRA v2.2	–
FWI	Fire weather index		
Popd	Population density (individuals km^{-2})	HYDE3.2	Klein Goldewijk et al. (2017)
LAI	Leaf area index in the previous months	TRENDY v11 GIMMS LAI4g	Cao et al. (2023); Sitch et al. (2024)
Forest	Fraction of certain land use type in $0.5° \times 0.5°$ grid cells in each year	LUH2-GCB2020 CCI PFT map	Chini et al. (2021); Li et al. (2018)
Shrub			
Natural Grass			
Cropland			
Δforest	Fraction difference of certain land use type in $0.5° \times 0.5°$ grid cells between the previous year and the current year		
Δshrub			
Δnatural grass			
Δcropland			
BAF	Burned area fraction in $0.5° \times 0.5°$ grid cells excluding burned area on cropland	FireCCI51	Lizundia-Loiola et al. (2020)

gradient boosting (Friedman, 2001) and extreme gradient boosting (Chen and Guestrin, 2016), and a deep learning architecture called long short-term memory networks (LSTMs) (Hochreiter and Schmidhuber, 1997) in NHAF and BOAS. We chose NHAF as the testing region because its annual total burned area dominates the global annual total burned area. Further, our preliminary tests severely underestimated the annual total burned area in NHAF, and thus we aimed to improve model performance in NHAF by testing different machine learning models. In this test, we took only one year's data (2010) and split it into the training set (80 %) and the testing set (20 %). In addition, we selected BOAS as another testing region because this region experiences regular fires but has different climatic and vegetation conditions from NHAF. In this test, we took only one year's data (2010) and split it into the training set (80 %) and the testing set (20 %). It turned out that LSTMs have the best performance (Figs. S7, S8, S10h, S11h) for regression with a memory window of three months. LSTMs consist of three gated memory cells (input gate, forget gate and output gate) that enable the integration of input data over long time series (Hochre-

iter and Schmidhuber, 1997), exhibiting good performance on extreme events (e.g., precipitation or floods) (de Sousa Araújo et al., 2022; Nearing et al., 2024). All machine learning models were built using the "scikit-learn" (Pedregosa et al., 2011) and "pytorch" (Paszke et al., 2019) packages in Python.

In addition to the 16 explanatory variables in Table 1, we conducted sensitivity tests by incorporating lightning (Kaplan and Lau, 2021) and terrain information (Danielson and Gesch, 2011) in each region (Sect. S3 in the Supplement) to assess whether these variables can help improve model performance. We also tested other variables in NHAF (e.g., gross domestic product, GDP; human development index, HDI; livestock density; road density; tree cover; and forest aboveground biomass) (Fig. S9), but they were excluded either using recursive feature elimination cross-validation (i.e., negligible contributions to the model) or due to the limited time span (i.e., not covering the entire 20th century and difficult to extrapolate). The recursive feature elimination cross-validation was applied to prevent model performance degradation if irrelevant features were added (Guyon and Elisse-

eff, 2003). Moreover, reducing the feature set could enhance model interpretability and conserve computational resources (Lundberg et al., 2020).

For the model parameterizations, the time step length was set to three consecutive months (the previous two months and the current month) in LSTMs to predict the current month's regular or extreme BAF. We randomly split the data over the period of 2003–2020 into five folds, using one fold (20 %) as the testing set and the remaining four folds as the training set (80 %). This process was looped for each of the five folds. We then used the training set to train the models and the testing set to evaluate model performance. We optimized the model parameters according to the principle of minimum Gini impurity for the classification model and minimum mean square error loss for the regressions. We optimized model hyperparameters using a grid search with five-fold cross-validation. For the random forest classifiers, we tuned "max_depth" and "n_estimators"; for the LSTM regressors, we tuned "hidden_sizes", "learning_rate" and "epochs". All combinations of these parameter values were used to retrain the models, and performance was evaluated on each held-out fold using coefficient of determination, slope, and rooted mean squared error. The combination yielding the best average metrics across folds was selected as optimal.

After determining the optimal model parameters, we conducted the model evaluation using a leave-one-year-out method in addition to the five-fold evaluation method in the model parameterization process. Specifically, for the period 2003–2020 in each region, we excluded one year's data and used data from the remaining years to train the models. The data from this year were then compared with the models' predictions for this year. This procedure was repeated for each year during 2003–2020. The SHapley Additive exPlanations (SHAP) value, representing the explainable contributions of features and their interactions in machine learning models, was calculated with the "shap" package (Lundberg et al., 2020) using TreeExplainer and DeepExplainer for the random forest classification models and LSTMs, respectively, in Python.

The machine learning models with optimal parameters from the five-fold evaluation process were finally used to predict global monthly BAF maps for 1901–2020. For the time series of annual total burned area, we conducted breakpoint detections and linear regressions for each segment. The number of breakpoints were identified using the Bayesian optimization function in the "GPyOpt" package (Javier Gonzalez, 2016), and linear regressions for each segment were conducted using the PiecewiseLinFit function in the "pwlf" package (Jekel and Venter, 2019) in Python.

2.3 Other fire datasets used for comparison

We used two databases of charcoal records, the Global Charcoal Database v4 (Power et al., 2010) and the Reading Palaeofire Database (Harrison et al., 2022) (D1 and D2 in Table 2),

to evaluate the models' prediction accuracy of fire occurrence from 1901 to 2020. Fire occurrence in a certain grid cell refers to its BAF being greater than 0, and we defined the prediction accuracy (%) for each site as the number of charcoal records that match our predicted fire occurrence divided by the total number of charcoal records multiplied by 100 %. Note that the charcoal age reported in both databases is associated with uncertainties, but only the Reading Palaeofire Database provides age uncertainties for some records. We thus calculated the average uncertainty across records with reported age uncertainties for 1901–2020 in the Reading Palaeofire Database and assigned this average uncertainty (3 years after rounding) to those records without reported uncertainties in both databases. For a given charcoal record, if there is a predicted fire occurrence in the same grid cell within the time span of the uncertainty age range, it is considered as a correct prediction.

In addition to the charcoal records databases, we compared our predicted burned area with burned area datasets in different countries or regions that cover more than 10 years (Table 2). Fire history reconstruction (D3 in Table 2) by Mouillot and Field (2005) is a global annual gridded ($1° \times 1°$) burned area dataset for the 20th century produced based on regional burned area statistics. The datasets by the State Government of Australia (D11–D14 in Table 2) include wildfires and prescribed burns, mainly consisting of bureau statistics and missing data before the satellite era and satellite-based data thereafter. The remaining polygon and raster datasets (burned area products across the globe and in Canada, the USA, Brazil, Chile and Europe) listed in Table 2 are all satellite-based. We converted the polygon data to raster data at a spatial resolution of 30 m and resampled all raster data to $0.5° \times 0.5°$. Then, we calculated the time series of annual and monthly total burned area in each region and globally. We also derived the spatial pattern averaged over all years of the reported period for each dataset.

3 Results

3.1 Model performance

In the optimization of model parameters (Sect. 2.2), the input data was randomly split into 80 % for training and 20 % for testing. Based this test subset, the overall accuracy of our random forest classification models range from 87.8 % to 97.7 % in the 14 regions. The ranges of AUC (area under the receiver operating characteristic curve, with values ranging between 0 and 1, and a higher values indicating better model performance) are 0.885–0.972 and 0.917–0.989 for grid cells with regular BAF and extreme BAF, respectively (Table S1 in the Supplement). Based on the testing samples, the slopes of the linear regression between the predicted and observed regular BAF across all grid cells in each region range from 0.42 to 0.96, and the coefficients of determination (R^2) range between 0.60 and 0.95 (Fig. S10). The slopes for the extreme

Table 2. Charcoal and burned area datasets used for comparison.

No.	Datasets	Spatial Resolution	Temporal Resolution	Source
D1	Global Charcoal Database	Global, site	B.P. 21 000-years	https://cran.r-project.org/web/packages/GCD/index.html (last access: 18 April 2024)
D2	Reading Palaeofire Database	Global, site	B.P. 56 000-years	Harrison et al. (2022)
D3	Fire history reconstruction for the 20th century	Global, $1° \times 1°$	1900–1999, annual	Mouillot and Field (2005)
D4	FireCCILT11	Global, $0.05° \times 0.05°$	1982–2018, monthly	Otón et al. (2021)
D5	Global Annual Burned Area Maps (GABAM)	Global, 30 m	1985–2020, annual	Long et al. (2019)
D6	Monitoring Trends in Burn Severity	USA, polygon	1984–2022, daily	Eidenshink et al. (2007)
D7	MapBiomas Fire Collection	Brazil, 30 m	1985–2020, annual	https://brasil.mapbiomas.org/en/mapbiomas-fogo/ (last access: 5 November 2022)
D8	Canadian National Burned Area Composite	Canada, polygon	1986–2022, daily	https://cwfis.cfs.nrcan.gc.ca/datamart (last access: 10 April 2024)
D9	European Forest Fire Information System	Europe, polygon	1980–2020, daily	https://forest-fire.emergency.copernicus.eu (last access: 28 August 2023)
D10	Occurrence of Wildfires by Time Range	Chile, polygon	1985–2020, annual	Chilean National Forest Service (CONAF)
D11	NPWS Wildfires and Prescribed Burns	New South Wales, polygon	1935–present, annual	https://data.nsw.gov.au/data/dataset/fire-history-wildfires-and-prescribed-burns-1e8b6 (last access: 14 April 2024)
D12	Fire history – Queensland Parks and Wildlife Service	Queensland, polygon	1937–present, annual	https://qldspatial.information.qld.gov.au/catalogue/custom (last access: 14 April 2024)
D13	Bushfires and Prescribed Burns History of South Australia	South Australia, polygon	1950–present, annual	https://data.sa.gov.au/data/dataset/fire-history (last access: 14 April 2024)
D14	DPCA Fire History of Western Australia	Western Australia, polygon	1926–present, annual	https://catalogue.data.wa.gov.au/dataset/dbca-fire-history (last access: 14 April 2024)

BAF are in the range 0.43–0.96, and R^2 is between 0.58 and 1 (Fig. S11).

In the model evaluation based on the leave-one-year-out method, the multi-year (2003–2020) mean BAF between observations (FireCCI51) and our prediction is spatially consistent in general. There is a strong spatial correlation between observations and predictions at the global scale, with a R^2 of 0.97 and a linear slope of 0.97. For all the regions, R^2 ranges from 0.69 to 0.98, and slopes range from 0.70 to 1.28 (Fig. 3a–o), which indicates that the trained models can well

reproduce the spatial patterns of burned area. Still, some regions show mismatches, especially in the tropics (Fig. 2a–b). Our predictions tend to overestimate BAF in the southeastern regions in South America (Figs. 2a, 3f) and in the southern part of Africa; however, they underestimate BAF in North Africa (Figs. 2a, 3i). Notably, the relative difference between predictions and observations is small in these regions. BAF in boreal North America and boreal Asia is also partially underestimated by our predictions (Figs. 2a, 3b, k). Large relative differences exist in the boreal regions compared with obser-

(a)

(b)
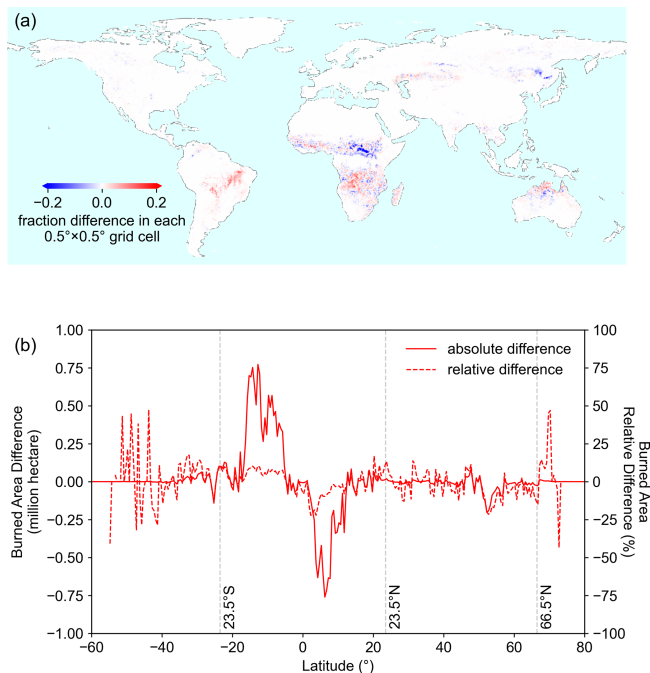
Figure 2. Multi-year (2003–2020) averaged burned area difference between our predictions by the leave-one-year-out method and FireCCI51 observations (predictions minus observations). **(a)** Map of the burned area fraction (BAF) difference in each $0.5° \times 0.5°$ grid cell. The BAF difference is the ratio of the burned area difference to the total grid area within each $0.5° \times 0.5°$ cell, making it unitless and bounded between 0 and 1. **(b)** Latitudinal sum of the burned area difference using the BAF difference map from **(a)** multiplied by the area of each $0.5° \times 0.5°$ grid cell. Both absolute (solid line) and relative (dashed line) differences are shown.

vations (Fig. 2b) due to the smaller absolute burned area than in the tropical regions. Additionally, the relative differences within 40–60° S fluctuate due to the small number of land grid cells with fire occurrence (Fig. 2b).

The interannual variabilities in global total burned area in 2003–2020 between the predictions and observations are in a good agreement at the global scale and within each region (Fig. S12). R^2 for the temporal regressions of the global total burned area between predictions and observations is 0.88, and it ranges from 0.43 to 0.99 across regions. The linear slope is 0.79 for the global total burned area, and its range is 0.54–1.24 across regions. The model can also well capture the seasonality of burned area in each region (Figs. S13, S14).

3.2 Variable importance for predicting burned area

We also analyzed variable importance based on the SHAP values for the burned area prediction. In terms of similarities in variable importance between the classification and regression models, fire weather index (FWI) and leaf area index (LAI) in the previous months are among the most important

variables in most regions, while the land use change fraction between the previous year and the current year (Δfraction) has low importance in all regions.

In the classification models built for distinguishing grid cells with no fire, regular BAF or extreme BAF (Fig. 4a), FWI and LAI, indicating climatic conditions and vegetation status, respectively, are the two most important predictors across the globe. Vapor pressure deficit (VPD) and daily maximum temperature (Tmax) are the most important climatic factors in boreal regions (BONA and BOAS). The area fractions of natural grass and cropland rank in the top 5 in MIDE, NHAF, CEAS and EQAS. The contribution of precipitation (Precip) is high in the tropical regions (NHSA, NHAF, SHAF and EQAS). Wind speed (Wind) is consistently not essential in all regions. The importance of population density (Popd) remains low in most regions except in EURO and CEAS.

In the regression models predicting regular BAF and extreme BAF (Fig. 4b, c), the contribution of FWI is more significant in predicting extreme BAF than regular BAF, while Tmax, VPD and LAI in the previous months are more crucial in predicting regular BAF than extreme BAF. Popd consistently shows a low contribution in predicting both regular BAF and extreme BAF. The cropland area fraction makes the largest contribution in NHAF and CEAS in predicting regular BAF, and forest area fraction is the most important variable for predicting extreme BAF in BONA and SEAS. Additionally, the shrub area fraction ranks in the top 5 for predicting extreme BAF in NHAF, SHSA and AUST.

3.3 Predicted burned area

The predicted annual global total burned area from 1901 to 2020 ranges from 3.46×10^6 to $4.58 \times 10^6 \, \mathrm{km^2 \, yr^{-1}}$, with regular and extreme burned area accounting for 1.36×10^6–1.74×10^6 and 2.00×10^6–$3.03 \times 10^6 \, \mathrm{km^2 \, yr^{-1}}$, respectively (Figs. S15a, S16a). In comparison, the global total burned area from FireCCI51 is in the range of 3.43×10^6–$4.58 \times 10^6 \, \mathrm{km^2 \, yr^{-1}}$ over 2003–2020 (1.43×10^6–1.71×10^6 and 1.99×10^6–$2.98 \times 10^6 \, \mathrm{km^2 \, yr^{-1}}$ for regular and extreme fires) (Figs. S15a, S16a). Breakpoint detection shows three segments with two breakpoints around 1978 and 2008 globally (Fig. 5a). Global total burned area decreased from 1901 to 1978 (slope $= -0.009 \times 10^6 \, \mathrm{km^2 \, yr^{-2}}$), increased from 1978 to 2008 (slope $= 0.020 \times 10^6 \, \mathrm{km^2 \, yr^{-2}}$) and then decreased again from 2008 to 2020 (slope $= -0.049 \times 10^6 \, \mathrm{km^2 \, yr^{-2}}$) (Fig. 5a). Extreme burned area mainly contributed to the above trends, with global total extreme burned area decreasing from 1901 to 1978 (slope $= -0.007 \times 10^6 \, \mathrm{km^2 \, yr^{-2}}$), increasing from 1978 to 2008 (slope $= 0.019 \times 10^6 \, \mathrm{km^2 \, yr^{-2}}$) and decreasing again from 2008 to 2020 (slope $= -0.047 \times 10^6 \, \mathrm{km^2 \, yr^{-2}}$) (Figs. S16a, S17a). Northern Hemisphere Africa (NHAF) and Southern Hemisphere Africa (SHAF) are the top two regions with the largest annual total burned area. The annual total burned area of NHAF is in the range
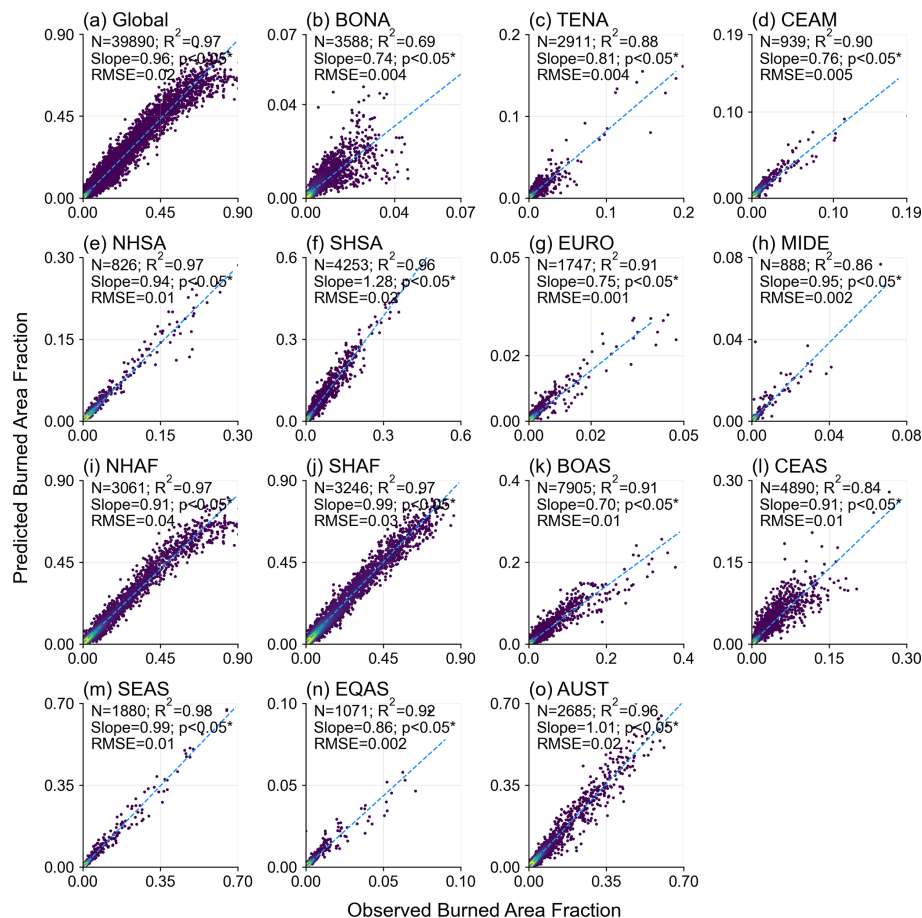
Figure 3. Scatter plots of the multi-year (2003–2020) averaged burned area fraction (BAF) in each $0.5° \times 0.5°$ grid cell from predictions by the leave-one-year-out method and FireCCI51 observations for each region **(a–o)**. Dots represent grid cells with BAF > 0 averaged over 2003–2020. N, R^2, slope, p and RMSE, respectively, represent the number of grid cells with multi-year averaged BAF > 0, coefficient of determination, linear slope, p-value for linear correlation and rooted mean squared error between the BAF from our predictions and observations. BAF is the ratio of burned area to total grid area within each $0.5° \times 0.5°$ cell, making it unitless and bounded between 0 and 1.

of 0.97×10^6–1.90×10^6 km^2 yr^{-1}, and it increased from 1901 to 1922 (slope $= 0.005 \times 10^6$ km^2 yr^{-2}), declined from 1922 to 1957 (slope $= -0.008 \times 10^6$ km^2 yr^{-2}) and then declined more slowly from 1957 to 2020 (slope $= -0.004 \times 10^6$ km^2 yr^{-2}) (Fig. 4i), dominated by extreme burned area (Figs. S16i, S17i). The annual total burned area of SHAF is in a similar range (1.15×10^6–1.87×10^6 km^2 yr^{-1}) as NHAF, and it also shows a similar decreasing trend from 1901 to 1979 (-0.004×10^6 km^2 yr^{-2}). However, it turned into an increasing trend from 1979 to 2011 (slope $= 0.011 \times 10^6$ km^2 yr^{-2}) and then decreased again from 2011 to 2020 (slope $= -0.019 \times 10^6$ km^2 yr^{-2}) (Fig. 5j), dominated by regular burned area (Figs. S16j, S17j). Therefore, the global burned area trends (Fig. 5a) are predominantly controlled by the trends in SHAF (Fig. 5j).

The total burned area in other tropical regions such as southern hemisphere South America (SHSA) and equatorial Asia (EQAS) is lower than that in Africa. The annual total burned area in SHSA is dominated by extreme burned area

(Fig. S17f) and varies from 0.09 to 0.66×10^6 km^2 yr^{-1}. It increased from 1901 to 1962 (slope $= 0.001 \times 10^6$ km^2 yr^{-2}), decreased with a slope of -0.002×10^6 km^2 yr^{-2} from 1962 to 1974 and then increased from 1974 to 2020 (0.004×10^6 km^2 yr^{-2}) (Fig. 5f). The annual total burned area in EQAS, dominated by extreme burned area (Fig. S17n), ranges from 0.002×10^6 to 0.018×10^6 km^2 yr^{-1}, but no significant trends were detected. In the boreal regions, the trends in annual total burned area are different between boreal North America (BONA) and boreal Asia (BOAS). The annual total burned area increased at 0.0003×10^6 km^2 yr^{-2} from 1901 to 1929, but it decreased at -0.0002×10^6 km^2 yr^{-2} from 1927 to 2017 in BONA (Fig. 5b). By contrast, it decreased at -0.0006×10^6 km^2 yr^{-2} from 1901 to 1941 but increased at 0.0009×10^6 km^2 yr^{-2} from 1941 to 1997 in BOAS (Fig. 5k).
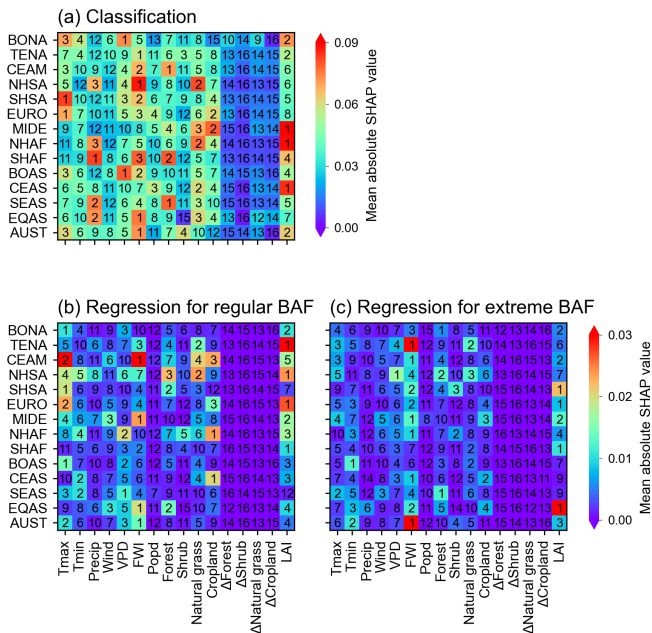
Figure 4. Mean absolute SHAP value and the ranking of all input variables (Table 1) using the random forest classification models **(a)** and the LSTM regression models for regular **(b)** and extreme **(c)** BAF, respectively, in each region. A higher ranking (i.e., smaller rank number and redder color) represents a relatively higher mean absolute SHAP value in the corresponding GFED region. The numbers denoted in grids are the ranking of the variables, and the colors denote mean absolute SHAP value in the corresponding GFED region.

## 3.4 Comparison with charcoal records and other burned area datasets

Two charcoal databases, Global Charcoal Database and Reading Palaeofire Database, were applied to calculate the overall accuracy (%) of the predicted fire occurrence. The overall accuracy of the two databases is 41.4 % ± 23.8 % and 33.0 % ± 15.3 % (average and standard deviation of the accuracy values for 1901–2020), respectively (Fig. 6c). Spatially, the number of sites in the Reading Palaeofire Database (Fig. 6b) is larger than that in the Global Charcoal Database (Fig. 6a). Sites with high accuracy (> 80 %) are mainly located in boreal North America, southern Europe, South America, Africa and southeast Australia (Fig. 6a, b). However, sites in northern Europe and Asia have relatively lower accuracy (< 50 %). In addition, Global Charcoal Database exhibits a significant increasing trend in global accuracy from 1901 to 2020, indicating better model performance in the recent period (Fig. 6c).

We further compared our predicted burned area with independent burned area datasets at the global and regional scale (Table 2). Significant trends in the annual total burned area in different regions from various datasets are summarized in Table S2.

At the global scale, we first compared our predictions with FireCCILT11, a satellite-based burned area dataset available monthly from 1982 to 2018 (1994 was missing) (Otón et al., 2021). Spatially, our predicted multi-year average BAF is lower than that reported by FireCCILT11 in regions such as CEAS, SEAS, Africa and the southern part of Australia (Fig. 7a). Consequently, the global and regional annual total burned area from our predictions is lower than that from FireCCILT11 (Fig. 8a–o). The global annual total burned area from our predictions ranges from 3.61×10^6 to 4.58×10^6 km^2 yr^{-1} during 1982–2018, compared to 4.09×10^6–5.18×10^6 km^2 yr^{-1} from FireCCILT11 over the same period. Significant linear trends were detected in the time series of annual total burned area from FireCCILT11 at the global scale and in CEAM, SHSA, MIDE, NHAF, SHAF and CEAS, and the trends are generally comparable to our predictions (Table S2). It should be noted, however, that significant orbit-drift artifacts may cause biases in the FireCCILT11 product over numerous large spatial patches almost on every continent except Antarctica (Giglio and Roy, 2022, 2024), and, thus, these comparisons should be interpreted with caution, especially in the tropics.

Next, we also compared our predictions with Global Annual Burned Area Maps (GABAM) (Long et al., 2019), a satellite-based burned area dataset available almost annually from 1985 to 2020 except for 1986, 1988, 1990, 1991, 1993, 1994, 1997 and 1999. Spatially, our predicted multi-year average BAF is higher than that in GABAM, mainly in the tropical regions (most Africa, Amazon and northern part of Australia) (Fig. 7b). This is because GABAM was produced from Landsat imagery, which has a lot of missing data in the tropics and thus underestimated burned area in these regions (Long et al., 2019; Pessôa et al., 2020). For 1985–2020, the global annual burned area from our predictions ranges 3.61×10^6–4.58×10^6 km^2 yr^{-1} compared to 0.77×10^6–4.90×10^6 km^2 yr^{-1} from GABAM. Regionally, annual total burned area from GABAM is consistent with our predictions for BONA, TENA, CEAM and EQAS (Fig. 8b–d, n), but it is much higher for EURO and MIDE (Fig. 8g, h). As a global dataset, neither evidence of active fires nor region-specific algorithms was taken into consideration in GABAM, which could also introduce uncertainty in burned area detection (Long et al., 2019).

We further compared our predictions with the fire reconstruction dataset by Mouillot and Field (2005) based on regional statistics. The multi-year average BAF from our predictions is lower than that from Mouillot and Field (2005) in the southeastern USA, SHSA, NHAF, India and Australia, but it is higher in SHAF and BOAS (Fig. 7c). The range of global annual total burned area during 1901–1999 is 3.46×10^6–4.51×10^6 km^2 yr^{-1} from our predictions, compared to 3.80×10^6–7.23×10^6 km^2 yr^{-1} from Mouillot and Field (2005) (Fig. 8a). At the global scale, annual total burned area increased by 0.020×10^6 km^2 yr^{-2} in 1978–2008 from our predictions and by 0.041×10^6 km^2 yr^{-2}
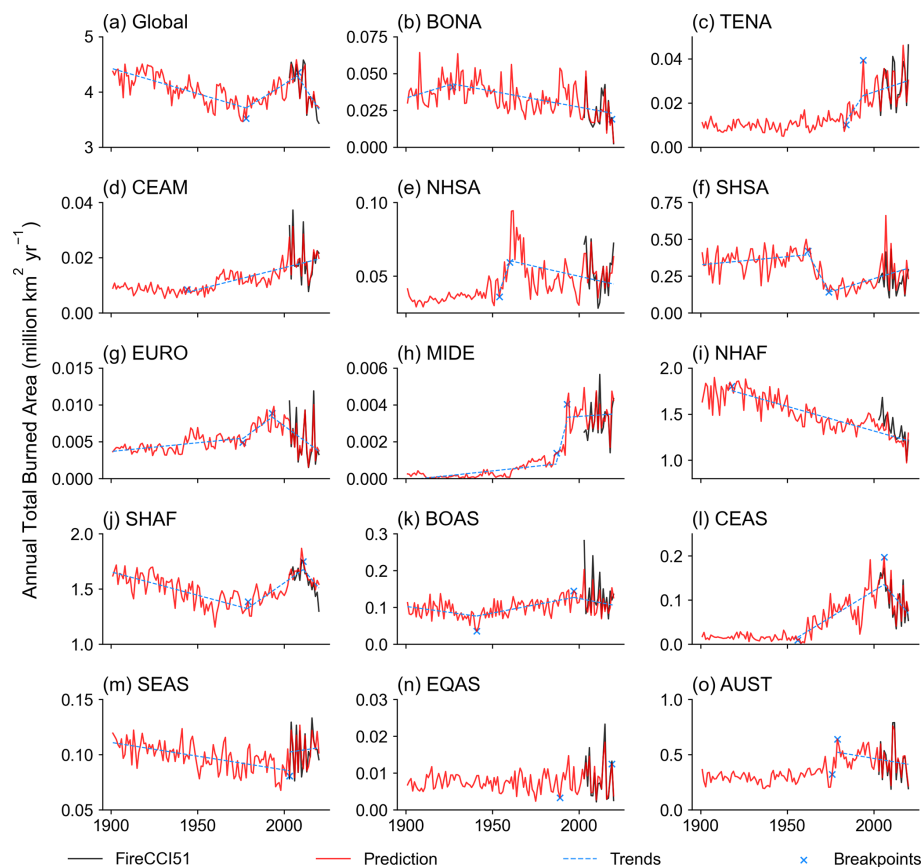
Figure 5. Time series of annual total burned area across the globe **(a)** and in each region **(b–o)** from FireCCI51 (black lines, 2003–2020) and predictions (red lines, 1901–2020). The breakpoints and significant slopes (p-value < 0.05) in blue are also shown (Sect. 2.2).

in 1972–1997 according to predictions from Mouillot and Field (2005), respectively (Fig. 8a). Annual total burned area from our predictions and Mouillot and Field (2005) exhibit similar trends in some regions. For example, the decreasing trend in annual total burned area in BONA during 1929–2017 from our predictions (Fig. 5b) is consistent with the trend during 1920–1965 from Mouillot and Field (2005) (Figs. 5b, 8b). In SHSA, similar increasing trends were detected during 1974–2020 from our predictions and during 1973–1999 from Mouillot and Field (2005) (Figs. 5f, 8f).

Comparing with the regional burned area datasets in Canada, the US (continental USA and Alaska), Brazil, Chile and Europe, the predictions generally reproduce the inter-annual variability of the total observed burned area (Fig. 9a–f). The slopes of the multi-year average burned area between our predictions and regional datasets range from 0.84 to 1.38, suggesting that they are in a good agreement spatially (Fig. 9k–p). Especially in Brazil and Chile, our predictions are highly consistent with the burned area from MapBiomas (D7, Table 2) and CONAF (D10, Table 2), respectively, based on the data from Landsat satellites, even in the period before 2000 when no burned area observations were used to train our models (Fig. 9d, e).

Our predicted burned area is higher than that from the regional datasets in the US and Europe before 2000 (Fig. 9b, f), probably because our model only included anthropogenic factors such as land use, land use change and population density, while fire management practices in these regions such as suppression were not explicitly included (Table 1). In Queensland and Western Australia (Fig. 9h, j), burned area from our predictions and FireCCI51 are both much higher than that reported by state governments (D11–D14, Table 2). Compared to the regional burned area datasets in Australia, our predictions are higher in the northern part but lower in the southern part (Fig. 9u). Although the time span of the burned area datasets in Australia is long, the incomplete statistics and missing data before the satellite era may also influence the reliability of these datasets.

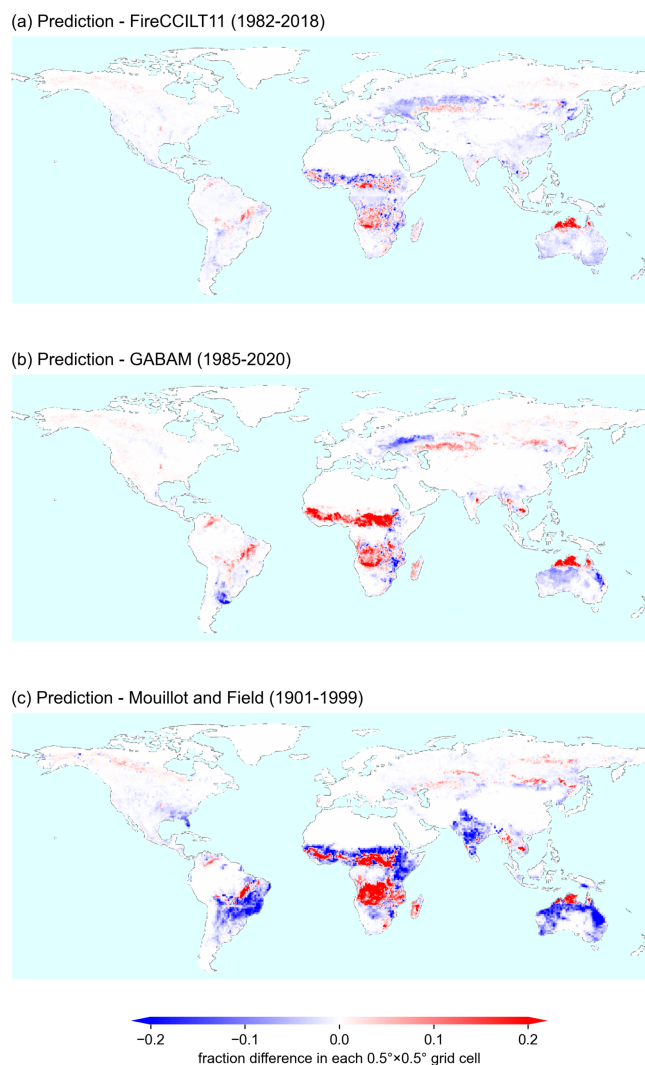### 3.5   Additional product versions

In addition to the historical reconstructed burned area dataset based on FireCCI51 presented above, we also produced two additional products of historical burned area with the same spatiotemporal resolution: (1) the GFED5-based version, which is based on machine-learning models trained on

(a)

(b)

(c)

△ Global Charcoal Database   ○ Reading Palaeofire Database
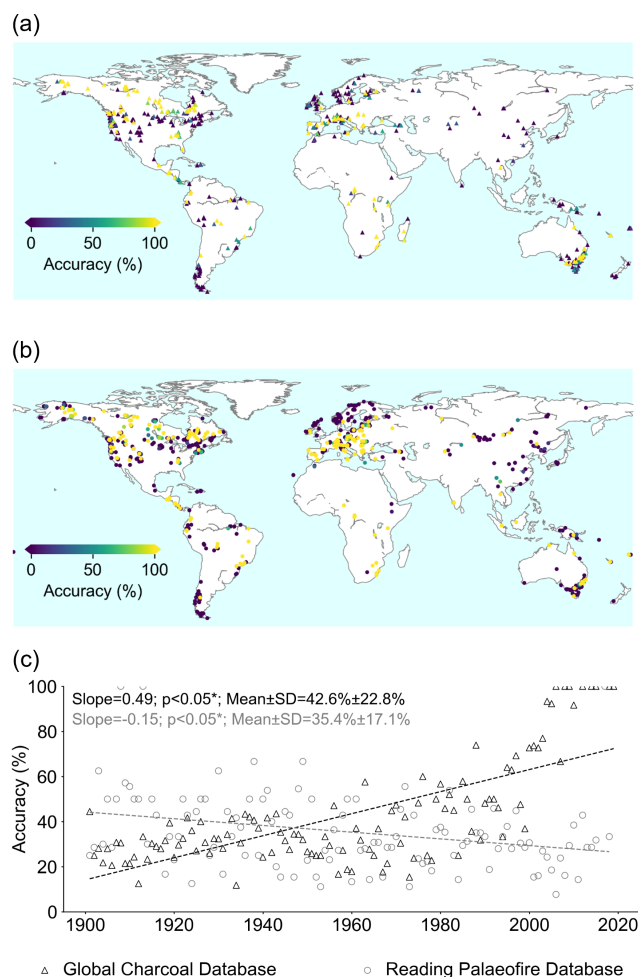
Figure 6. Fire occurrence comparison between two charcoal record databases and our prediction from 1901 to 2020. **(a)** Site accuracy map using the Global Charcoal Database. The site accuracy (%) is equal to the number of records with predicted burned area divided by the number of all records and multiplying by 100 %. **(b)** The same as **(a)** but using the Reading Palaeofire Database instead. **(c)** Accuracy time series using the Global Charcoal Database and Reading Palaeofire Database, respectively. Note that only records with record year ± record age uncertainty overlapping with 1901–2020 are taken into consideration.

(a) Prediction - FireCCILT11 (1982-2018)

(b) Prediction - GABAM (1985-2020)

(c) Prediction - Mouillot and Field (1901-1999)

Figure 7. Maps of burned area fraction difference between our predictions and other global burned area datasets. **(a)** Map of the multi-year average (1982–2018) burned area fraction difference between our predictions and FireCCILT11 (the former minus the latter). **(b, c)** Same as **(a)** but using the Global Annual Burned Area Maps (GABAM) (1985–2020) and Mouillot and Field (2005) (1901–1999), respectively. Note that there are several years (1986, 1988, 1990, 1991, 1993, 1994, 1997 and 1999) without available data before 2000 in GABAM.

the burned area from GFED5, which includes much more fires than GFED4 (Chen et al., 2023) instead of FireCCI51, and (2) FireCCI51-GDP-based version, with burned area further calibrated using the relationship between statistically derived burned area (Mouillot and Field, 2005) and regional gross domestic product (GDP) (Bolt and van Zanden, 2024) before 2000.

The GFED5-based version was produced and validated using the same methods as in Sect. 2.1 and 2.2 but by replacing the burned area of FireCCI51 with GFED5. The GFED5 burned area is based on the MCD64A1 burned area and adjusted with the Landsat or Sentinel-2 data, includ-

ing more small fires in this product (Chen et al., 2023). The evaluation results of the GFED5-based reconstruction are explicitly described in Sect. S1 (Figs. S18–S20). Briefly, the annual global total burned area in the GFED5-based version for 1901–2020 ranges from 5.42×10^6 to $7.35 \times 10^6 \, \text{km}^2 \, \text{yr}^{-1}$, with regular and extreme burned area accounting for 2.72×10^6–$3.13 \times 10^6 \, \text{km}^2 \, \text{yr}^{-1}$ and 2.54×10^6–$4.27 \times 10^6 \, \text{km}^2 \, \text{yr}^{-1}$, respectively (Figs. S21a, S22a, S23a), compared to the range of 3.46×10^6–$4.58 \times 10^6 \, \text{km}^2 \, \text{yr}^{-1}$ over 1901–2020 (1.36×10^6–1.74×10^6 and 2.00×10^6–$3.03 \times 10^6 \, \text{km}^2 \, \text{yr}^{-1}$ for regular and extreme fires) in the FireCCI51-
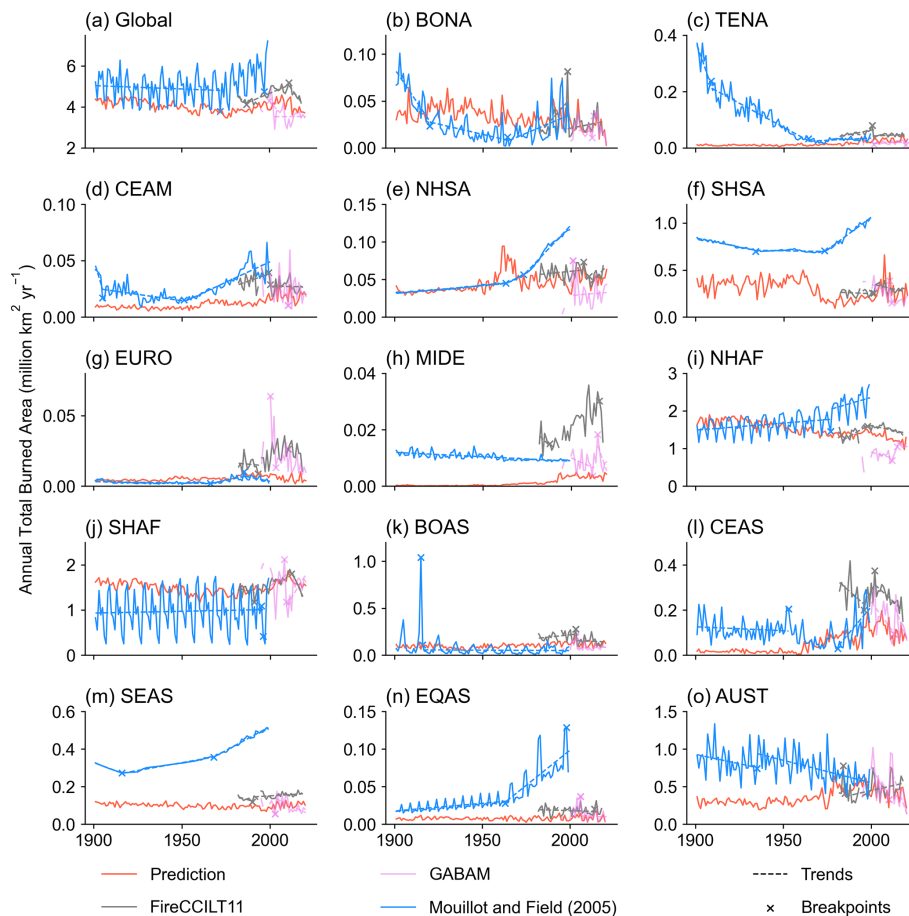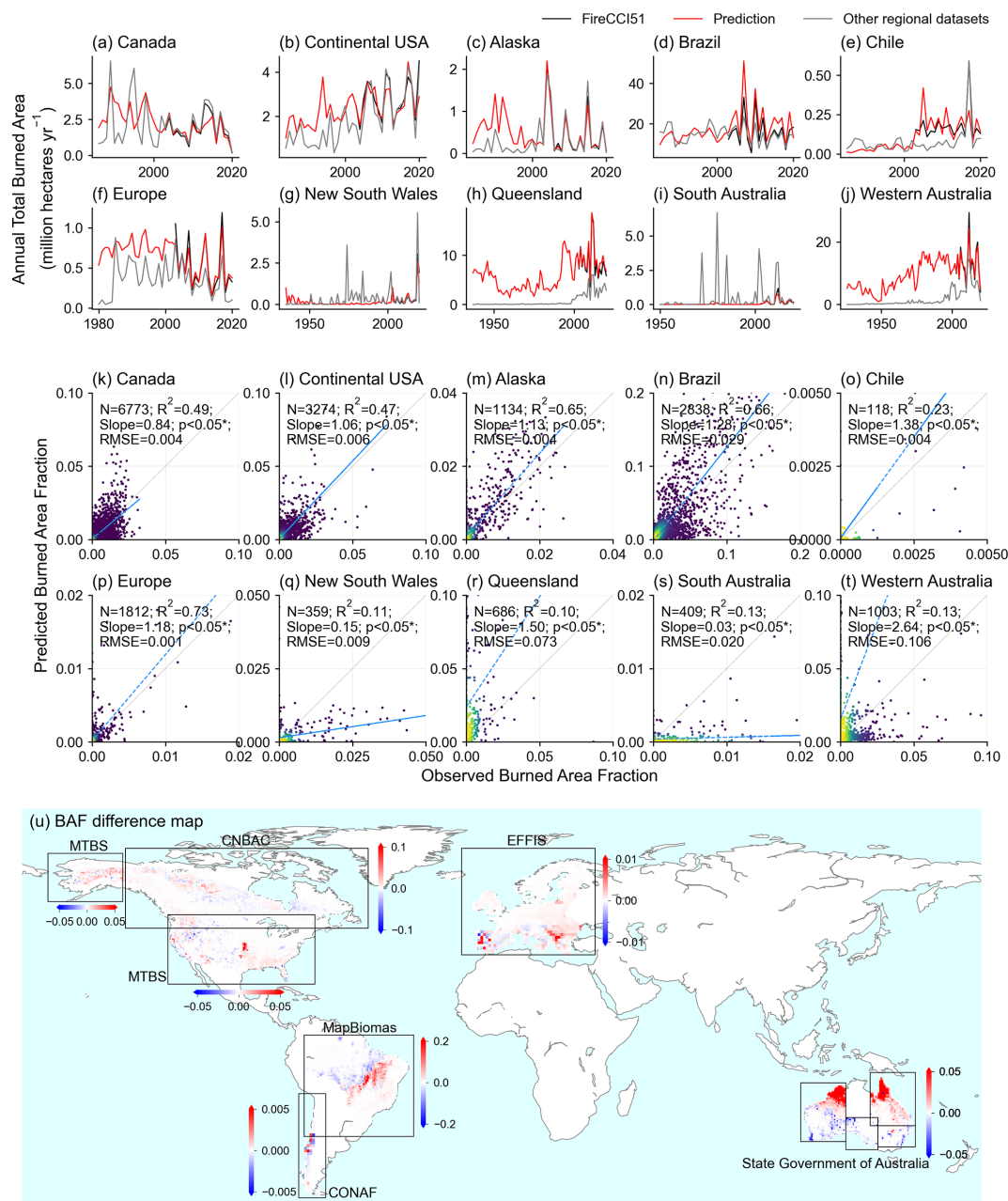
Figure 8. Time series of the annual total burned area across the globe **(a)** and in each region **(b–o)** from our predictions (red lines), Mouillot and Field (2005) (blue lines), FireCCILT11 (gray lines) and GABAM (purple lines). The breakpoints and significant slopes (p-value < 0.05) were calculated using the methods mentioned in Sect. 2.2. Note that there are several years (1986, 1988, 1990, 1991, 1993, 1994, 1997 and 1999) without available data before 2000 in GABAM, and thus breakpoint detection and linear slopes were applied after 2000 for this dataset.

based reconstruction (Figs. S15a, S16a). In most regions, despite the annual total burned area from the GFED5-based reconstruction being generally higher than that from the FireCCI51-based reconstruction due to differences in data sources (e.g., more small fires from GFED5), the trends in annual total burned area from both reconstructions are generally consistent across different regions (Fig. S21). However, one main difference between these two data versions is that the decreasing trend in global annual total burned area in the first half of the 20th century disappears in the GFED5-based reconstruction (Fig. S21a) because of the diminished decreasing trend in SHAF (Fig. S21j).

To explicitly consider more anthropogenic effects (e.g., fire suppression or landscape fragmentation), in addition to the population density used in the original FireCCI51-based reconstruction, we also calibrated the reconstructed burned area before 2000 at the regional scale using GDP as a proxy for anthropogenic effects and the statistic-based burned area from Mouillot and Field (2005) (see detailed methods in Sect. S2 and Fig. S24). Temporally, the annual global to-

tal burned area in the FireCCI51-GDP data version before 2000 ranges from 4.77×10^6 to 6.44×10^6 km^2 yr^{-1}, with regular and extreme burned area accounting for 1.68×10^6–2.31×10^6 km^2 yr^{-1} and 2.87×10^6–4.29×10^6 km^2 yr^{-1}, respectively (blue lines in Figs. S21a, S22a, S23a). The area is much larger than the global total burned area from the original FireCCI51-based version, which ranges between 3.46×10^6–4.51×10^6 km^2 yr^{-1} before 2000 (1.41×10^6–1.74×10^6 and 2.00×10^6–2.95×10^6 km^2 yr^{-1} for regular and extreme fires) (Figs. S15a, S16a). The temporal trends in annual total burned area in the FireCCI51-GDP version is similar to the original FireCCI51-based version in most regions. However, the trends in TENA (Fig. S21c), NHAF (Fig. S21i) and AUST (Fig. S21o) are opposite between the FireCCI51-GDP version and the original FireCCI51-based version. This could be partly explained by the trends in annual total burned area from Mouillot and Field (2005) (Fig. 8i, o), which was used to build the relationship between regional burned area and GDP. The regional total burned area after calibration using GDP was applied proportionally to each grid cell based on

Figure 9. Burned area comparison between our predictions and other regional burned area datasets. **(a–j)** Time series of the annual total burned area from FireCCI51 (black lines), our predictions (red lines) and other regional datasets (gray lines). **(k–t)** Scatter plots comparing burned area fractions from our predictions and other regional datasets using multi-year averaged values (the full time span of observations). **(u)** Map of the multi-year average burned area difference between our predictions and other regional datasets (the former minus the latter). The labels next to each rectangle correspond to the abbreviated names of the datasets in Table 2. Note that the scales of the color bars are different across regions.

the gridded burned area from the original FireCCI51-based version (Sect. S2). As a result, the spatial patterns remain similar between these two data versions.

4 Uncertainty and discussion

Although our models show good performance in the evaluation (Figs. 2–3, S10–S13), there are some uncertainties in the reconstructed historical burned area product, associated with the input explanatory data, the satellite-based burned area

used for model training and the model selection. Due to the limited time span of the satellite-based data, such as that on land use change and LAI, we harmonized the satellite-based datasets with other datasets before the satellite era. For example, large regional and global differences were found between the two land use datasets (LUH2-GCB2020 and CCI plant functional type (PFT) maps) (Fig. S3). Different data sources, definitions of land use types and uncertainties in the cross-walking table for converting the 37 original ESA CCI land cover types to the main land cover classes may partly explain the differences between the two land use datasets (Li et al., 2018). There are several alternative land cover and land use datasets with a higher spatial resolution than ESA CCI and LUH2-GCB2020, such as forest maps (Hansen et al., 2013; Vancutsem et al., 2021) and global cropland extent maps (Potapov et al., 2022). However, due to the limited temporal coverage or land cover types, we used ESA CCI and LUH2-GCB2020 for their consistent and comprehensive land cover and land use types and the long temporal coverage. Differences also exist between the two LAI datasets (GIMMS LAI4g and LAI from TRENDY v11) (Figs. S5, S6) due to differences in data sources. GIMMS LAI4g is a satellite-based product (Cao et al., 2023), while the LAI from TRENDY v11 was simulated by DGVMs (Sitch et al., 2024). In addition to the features selected in this study, other variables besides those listed in Table 2 were tested but eliminated (Fig. S9, Tables S3–S5). For instance, lightning data are only available for 2010–2024, and thus they cannot be utilized to reconstruct burned area in the 20th century (Kaplan and Lau, 2021). Terrain resampling to $0.5° \times 0.5°$ grid cells inevitably diluted explicit information from a fine spatial resolution (Cary et al., 2006), thus posing a minor effect across all regions except NHAF and SHAF. GDP and HDI (Kummu et al., 2018) were not important in the sensitivity tests probably because they were produced with sub-national data and mapped based on the same population density data as we used (Table 1). Other tested variables (e.g., livestock density, road density, forest aboveground biomass and tree cover) were excluded due to their low importance, the limited temporal coverage of data sources and difficulty in extrapolation (Gilbert et al., 2018; Hansen et al., 2013; Meijer et al., 2018; Santoro et al., 2021). Sea-surface temperature has also been proved as a good indicator of El Niño–Southern Oscillation (ENSO) and fire activity, especially in the tropics (Chen et al., 2011; Fernandes et al., 2011). However, our model training and prediction are based on land grid cells, and it is difficult to incorporate the sea-surface temperature information in each land grid cell in the current framework. In addition, sea-surface temperature is closely linked to climate variables over land through atmospheric circulation and teleconnection. Thus, the impacts of sea-surface temperature could have been implicitly considered in the model through the climate variables over land. Representations of anthropogenic interventions on fires (e.g., fire suppression or prescribed burns) (Libonati, 2024) cannot be fully considered by

the population density used in our models due to the limited temporal coverage of the related datasets. Fire suppression has been used to historically control fire activities for a long time (Douglas et al., 2001), especially in the US. About 98 % of wildfires were suppressed within the first 24 h in the US (Calkin et al., 2005). Meanwhile, evidence shows that conventional fire suppression can build up fuels and enlarge fire risk. Thus, prescribed burns are the new recognized measure for clearing accumulated fuels and relieving extreme wildfire risk (Kreider et al., 2024; Schoennagel et al., 2017). Unfortunately, fire suppression was not explicitly represented in our models due to a lack of data, and it may partly explain the overestimated burned areas in continental USA and Europe during the 20th century (Fig. 9b, g). Moreover, landscape fragmentation, usually caused by land use and management (Driscoll et al., 2021), has also been proved to alter fire regimes (Alencar et al., 2015), fire occurrence (Silva Junior et al., 2018) and burned area trends (Rosan et al., 2022) in some regions. Nevertheless, fragmentation was not explicitly considered in the reconstruction of burned area in this study, because fragmentation indices are calculated based on high-resolution land cover maps, and there are no such data available before the satellite era.

Though the temporal coverage of FireCCILT11 is longer than that of FireCCI51, there are some known issues in FireCCILT11. For example, the orbit-drift artifacts can be many times greater in magnitude than the true burned area signal, especially in the tropics and the USA, and it thus distorts burned area trends and causes inconsistency over the time span at the sub-continental scale (Giglio and Roy, 2022, 2024). We chose to use FireCCI51 for its recognized coherence and robust performance, but FireCCI51 may neglect some small fires due to its moderate spatial resolution (approximately 250 m), even though the sensitivity to small fires in FireCC51 was improved compared with FireCCI50 (Lizundia-Loiola et al., 2020).

In this study, we tested other commonly used machine learning models in NHAF and BOAS (Sect. 2.2). In NHAF, the R^2 between the BAF observations and BAF predictions by other machine learning models is 0.54 for regular BAF and ranges from 0.29 to 0.33 for extreme BAF (Fig. S7). LSTMs performed best with a R^2 of 0.78 for regular BAF and 0.69 for extreme BAF (Figs. S10h, S11h). In BOAS, the R^2 between observations and predictions by other machine learning models is 0.59–0.74 for regular BAF (Fig. S8b–e) and 0.36–0.53 for extreme BAF (Fig. S8g–j). LSTMs performed best with a R^2 of 0.75 for regular BAF and 0.56 for extreme BAF (Fig. S8a, f). Compared with models only using information at the current time step, LSTMs incorporate information from previous time steps and thus are able to include feedback effects from output to input, which is important to account for the complex interactions between fires and other factors (Hochreiter and Schmidhuber, 1997). Extrapolation studies are based on the assumption that the paradigms of the interacting factors will not change in space or time, so

models trained on limited data can be applied to make predictions beyond the spatial or temporal coverage of the training data. However, the paradigms may change across space or time in the real world. Therefore, this kind of uncertainty inevitably exists spatiotemporally in extrapolation studies.

When comparing fire occurrence with charcoal datasets, the varying accuracy across the globe could partially be explained by the varying data quality across sites. Meanwhile, there are large uncertainties in the models used for calculating the age of charcoal records (Harrison et al., 2022), which affect the calculation of predicted fire occurrence accuracy to some degree. Moreover, charcoal records could not distinguish wildfires and human-induced fires, but our predictions exclude fires in croplands (Sect. 2.1), which may cause inconsistency between charcoal records and our reconstruction. The differences between our predictions and the dataset by Mouillot and Field (2005) may also be induced by some assumptions (e.g., applying the same trends to nearby countries if there is no historical data, or using a prescribed fire probability map for burned area mapping) in Mouillot and Field (2005) due to a lack of data and some methodology limitations. Moreover, some burned area statistics before the satellite era in some regions (e.g., US Forest Services, Food and Agriculture Organization of the United Nations) applied in Mouillot and Field (2005) could be very uncertain due to the difficulty in counting all fires across a country or state without large-scale monitoring techniques. In summary, our predictions reproduced the inter-annual variability and seasonality of FireCCI51 (2003–2020) in all regions, and match well with other observation-based burned area datasets in Brazil and Chile (1985–2020), even though we fed no observed burned area before the 21st century to train our models. Our predictions are yet able to capture the spatiotemporal pattern of burned area in some regions (e.g., Australia) due to the uncertainty and missing data from data sources.

5   Data availability

The global monthly $0.5° \times 0.5°$ burned area fraction maps from 1901 to 2020 can be freely accessed at https://doi.org/10.5281/zenodo.14191467 (Guo and Li, 2024). The availability of other datasets used in this study is noted in Tables 1 and 2.

6   Conclusions

We used machine learning models to build empirical relationships between monthly burned area fraction and factors related to climate, vegetation and human activities at the $0.5° \times 0.5°$ scale. Our historical burned area product (1901–2020) can be used to benchmark historical fire module simulations in DGVMs, re-calculate historical fire emissions and estimate the legacy effects of vegetation recovery after fires on the terrestrial carbon sink. Though the temporal coverage of our product is long enough to support studies related to fire disturbance, carbon dynamics and climate change, more reliable explanatory data for model training, and burned area data for validation, would help further improve the accuracy of the reconstructed burned area product.

Author contributions. ZG conducted data analysis, produced the dataset and drafted the manuscript. WL and PC proposed the idea and supervised the study. SS and GRW provided necessary datasets for this study. WL and ZG revised the manuscript, with PC, SS, GRW, SPKB, AB, FM and XH contributing to methodological improvements and revision of the manuscript. JH, MS, LZ, XD and NW helped collect data and check the results.

References

Alencar, A. A., Brando, P. M., Asner, G. P., and Putz, F. E.: Landscape fragmentation, severe drought, and the new Amazon forest fire regime, Ecol. Appl., 25, 1493–1505, https://doi.org/10.1890/14-1528.1, 2015.

Andela, N., Morton, D. C., Giglio, L., Chen, Y., van der Werf, G. R., Kasibhatla, P. S., DeFries, R. S., Collatz, G. J., Hantson, S., Kloster, S., Bachelet, D., Forrest, M., Lasslop, G., Li, F., Mangeon, S., Melton, J. R., Yue, C., and Randerson, J. T.: A human-driven decline in global burned area, Science, 356, 1356–1362, https://doi.org/10.1126/science.aal4108, 2017.

Bolt, J. and van Zanden, J. L.: Maddison-style estimates of the evolution of the world economy: A new 2023 update, J. Econ. Surv., 39, 631–671, https://doi.org/10.1111/joes.12618, 2024.

Bond, W. J., Woodward, F. I., and Midgley, G. F.: The global distribution of ecosystems in a world without fire, New Phytol., 165, 525–538, https://doi.org/10.1111/j.1469-8137.2004.01252.x, 2005.

Bowman, D. M. J. S., Balch, J. K., Artaxo, P., Bond, W. J., Carlson, J. M., Cochrane, M. A., D'Antonio, C. M., DeFries, R. S., Doyle, J. C., Harrison, S. P., Johnston, F. H., Keeley, J. E., Krawchuk, M. A., Kull, C. A., Marston, J. B., Moritz, M. A., Prentice, I. C., Roos, C. I., Scott, A. C., Swetnam, T. W., van der Werf, G. R., and Pyne, S. J.: Fire in the Earth System, Science, 324, 481–484, https://doi.org/10.1126/science.1163886, 2009.

Bowman, D. M. J. S., Williamson, G. J., Abatzoglou, J. T., Kolden, C. A., Cochrane, M. A., and Smith, A. M. S.: Human exposure and sensitivity to globally extreme wildfire events, Nat. Ecol. Evol., 1, 0058, https://doi.org/10.1038/s41559-016-0058, 2017.

Bowman, D. M. J. S., Kolden, C. A., Abatzoglou, J. T., Johnston, F. H., van der Werf, G. R., and Flannigan, M.: Vegetation fires in the Anthropocene, Nature Reviews Earth & Environment, 1, 500–515, https://doi.org/10.1038/s43017-020-0085-3, 2020.

Breunig, M. M., Kriegel, H.-P., Ng, R. T., and Sander, J.: LOF: identifying density-based local outliers, Proceedings of the 2000 ACM SIGMOD international conference on Management of data, Dallas, Texas, USA, https://doi.org/10.1145/342009.335388, 2000.

Buck, A. L.: New Equations for Computing Vapor Pressure and Enhancement Factor, J. Appl. Meteorol., 20, 1527–1532, 1981.

Calkin, K., Gebert, M., Jones, J. G., Neilson, R. P.: Forest Service Large Fire Area Burned and Suppression Expenditure Trends, 1970–2002, J. Forestry, 103, 179–183, https://doi.org/10.1093/jof/103.4.179, 2005.

Cao, S., Li, M., Zhu, Z., Wang, Z., Zha, J., Zhao, W., Duanmu, Z., Chen, J., Zheng, Y., Chen, Y., Myneni, R. B., and Piao, S.: Spatiotemporally consistent global dataset of the GIMMS leaf area index (GIMMS LAI4g) from 1982 to 2020, Earth Syst. Sci. Data, 15, 4877–4899, https://doi.org/10.5194/essd-15-4877-2023, 2023.

Cary, G. J., Keane, R. E., Gardner, R. H., Lavorel, S., Flannigan, M. D., Davies, I. D., Li, C., Lenihan, J. M., Rupp, T. S., and Mouillot, F.: Comparison of the Sensitivity of Landscape-fire-succession Models to Variation in Terrain, Fuel Pattern, Climate and Weather, Landscape Ecol., 21, 121–137, https://doi.org/10.1007/s10980-005-7302-9, 2006.

Castro Rego, F., Morgan, P., Fernandes, P., and Hoffman, C.: Extreme Fires, in: Fire Science: From Chemistry to Landscape Management, edited by: Rego, F. C., Morgan, P., Fernandes, P., and Hoffman, C., Springer International Publishing, Cham, 175–257, https://doi.org/10.1007/978-3-030-69815-7_8, 2021.

Chen, T. and Guestrin, C.: XGBoost: A Scalable Tree Boosting System, Proceedings of the 22nd ACM SIGKDD International Conference on Knowledge Discovery and Data Mining, San Francisco, California, USA, https://doi.org/10.1145/2939672.2939785, 2016.

Chen, Y., Randerson, J. T., Morton, D. C., DeFries, R. S., Collatz, G. J., Kasibhatla, P. S., Giglio, L., Jin, Y., and Marlier, M. E.: Forecasting Fire Season Severity in South America Using Sea Surface Temperature Anomalies, Science, 334, 787–791, https://doi.org/10.1126/science.1209472, 2011.

Chen, Y., Hall, J., van Wees, D., Andela, N., Hantson, S., Giglio, L., van der Werf, G. R., Morton, D. C., and Randerson, J. T.: Multi-decadal trends and variability in burned area from the fifth version of the Global Fire Emissions Database (GFED5), Earth Syst. Sci. Data, 15, 5227–5259, https://doi.org/10.5194/essd-15-5227-2023, 2023.

Chini, L., Hurtt, G., Sahajpal, R., Frolking, S., Klein Goldewijk, K., Sitch, S., Ganzenmüller, R., Ma, L., Ott, L., Pongratz, J., and Poulter, B.: Land-use harmonization datasets for annual global carbon budgets, Earth Syst. Sci. Data, 13, 4175–4189, https://doi.org/10.5194/essd-13-4175-2021, 2021.

Chuvieco, E., Mouillot, F., van der Werf, G. R., San Miguel, J., Tanase, M., Koutsias, N., García, M., Yebra, M., Padilla, M., Gitas, I., Heil, A., Hawbaker, T. J., and Giglio, L.: Historical background and current developments for mapping burned area from satellite Earth observation, Remote Sens. Environ., 225, 45–64, https://doi.org/10.1016/j.rse.2019.02.013, 2019.

Clarke, H., Nolan, R. H., De Dios, V. R., Bradstock, R., Griebel, A., Khanal, S., and Boer, M. M.: Forest fire threatens global carbon sinks and population centres under rising atmospheric water demand, Nat. Commun., 13, 7161, https://doi.org/10.1038/s41467-022-34966-3, 2022.

Cunningham, C. X., Williamson, G. J., and Bowman, D. M. J. S.: Increasing frequency and intensity of the most extreme wildfires on Earth, Nature Ecol. Evol., 8, 1420–1425, https://doi.org/10.1038/s41559-024-02452-2, 2024.

Danielson, J. J. and Gesch, D. B.: Global multi-resolution terrain elevation data 2010 (GMTED2010), Report 2011-1073, https://doi.org/10.3133/ofr20111073, 2011.

de Sousa Araújo, A., Silva, A. R., and Zárate, L. E.: Extreme precipitation prediction based on neural network model – A case study for southeastern Brazil, J. Hydrol., 606, 127454, https://doi.org/10.1016/j.jhydrol.2022.127454, 2022.

Douglas, J., Mills, T. J., Artly, D., Ashe, D., Bartuska, A., Black, R. L., Coloff, S., Cruz, J., Edrington, M., Edwardson, J., Gale, R. T., Goodman, S. W., Hamilton, L., Landis, R., Powell, B., Robinson, S., Schuster, R. J., Stahlschmidt, P. K., Stires, J., and van Wagtendonk, J.: Review and update of the 1995 Federal wildland fire management policy, Report, 78-, 2001.

Driscoll, D. A., Armenteras, D., Bennett, A. F., Brotons, L., Clarke, M. F., Doherty, T. S., Haslem, A., Kelly, L. T., Sato, C. F., Sitters, H., Aquilué, N., Bell, K., Chadid, M., Duane, A., Meza-Elizalde, M. C., Giljohann, K. M., González, T. M., Jambhekar, R., Lazzari, J., Morán-Ordóñez, A., and Wevill, T.: How fire interacts with habitat loss and fragmentation, Biol. Rev., 96, 976–998, https://doi.org/10.1111/brv.12687, 2021.

Eidenshink, J., Schwind, B., Brewer, K., Zhu, Z.-L., Quayle, B., and Howard, S.: A Project for Monitoring Trends in Burn Severity, Fire Ecol., 3, 3–21, https://doi.org/10.4996/fireecology.0301003, 2007.

Fernandes, K., Baethgen, W., Bernardes, S., DeFries, R., DeWitt, D. G., Goddard, L., Lavado, W., Lee, D. E., Padoch, C., Pinedo-Vasquez, M., and Uriarte, M.: North Tropical Atlantic influence on western Amazon fire season variability, Geophys. Res. Lett., 38, L12701, https://doi.org/10.1029/2011GL047392, 2011.

Flannigan, M. D., Krawchuk, M. A., de Groot, W. J., Wotton, B. M., and Gowman, L. M.: Implications of changing climate for global wildland fire, Int. J. Wildland Fire, 18, 483–507, 2009.

Friedman, J. H.: Greedy function approximation: a gradient boosting machine, Ann. Stat., 29, 1189–1232, 2001.

Giglio, L. and Roy, D. P.: Assessment of satellite orbit-drift artifacts in the long-term AVHRR FireCCILT11 global burned area data set, Sci. Remote Sens., 5, 100044, https://doi.org/10.1016/j.srs.2022.100044, 2022.

Giglio, L. and Roy, D. P.: Satellite artifacts modulate FireC-CILT11 global burned area, Nat. Commun., 15, 2079, https://doi.org/10.1038/s41467-024-46168-0, 2024.

Giglio, L., van der Werf, G. R., Randerson, J. T., Collatz, G. J., and Kasibhatla, P.: Global estimation of burned area using MODIS active fire observations, Atmos. Chem. Phys., 6, 957–974, https://doi.org/10.5194/acp-6-957-2006, 2006.

Gilbert, M., Nicolas, G., Cinardi, G., Van Boeckel, T. P., Van-wambeke, S. O., Wint, G. R. W., and Robinson, T. P.: Global distribution data for cattle, buffaloes, horses, sheep, goats, pigs, chickens and ducks in 2010, Sci. Data, 5, 180227, https://doi.org/10.1038/sdata.2018.227, 2018.

Guo, Z. and Li, W.: Reconstructed Global Monthly Burned Area Maps from 1901 to 2020, Zenodo [data set], https://doi.org/10.5281/zenodo.14191467, 2024.

Guyon, I. and Elisseeff, A.: An introduction to variable and feature selection, J. Mach. Learn. Res., 3, 1157–1182, 2003.

Hansen, M. C., Potapov, P. V., Moore, R., Hancher, M., Turubanova, S. A., Tyukavina, A., Thau, D., Stehman, S. V., Goetz, S. J., Loveland, T. R., Kommareddy, A., Egorov, A., Chini, L., Justice, C. O., and Townshend, J. R. G.: High-Resolution Global Maps of 21st-Century Forest Cover Change, Science, 342, 850–853, https://doi.org/10.1126/science.1244693, 2013.

Hantson, S., Kelley, D. I., Arneth, A., Harrison, S. P., Archibald, S., Bachelet, D., Forrest, M., Hickler, T., Lasslop, G., Li, F., Mangeon, S., Melton, J. R., Nieradzik, L., Rabin, S. S., Prentice, I. C., Sheehan, T., Sitch, S., Teckentrup, L., Voulgarakis, A., and Yue, C.: Quantitative assessment of fire and vegetation properties in simulations with fire-enabled vegetation models from the Fire Model Intercomparison Project, Geosci. Model Dev., 13, 3299–3318, https://doi.org/10.5194/gmd-13-3299-2020, 2020.

Harris, I., Jones, P. D., Osborn, T. J., and Lister, D. H.: Updated high-resolution grids of monthly climatic observations – the CRU TS3.10 Dataset, Int. J. Climatol., 34, 623–642, https://doi.org/10.1002/joc.3711, 2014.

Harris, I., Osborn, T. J., Jones, P., and Lister, D.: Version 4 of the CRU TS monthly high-resolution gridded multivariate climate dataset, Sci. Data, 7, 109, https://doi.org/10.1038/s41597-020-0453-3, 2020.

Harrison, S. P., Villegas-Diaz, R., Cruz-Silva, E., Gallagher, D., Kesner, D., Lincoln, P., Shen, Y., Sweeney, L., Colombaroli, D., Ali, A., Barhoumi, C., Bergeron, Y., Blyakharchuk, T., Bobek, P., Bradshaw, R., Clear, J. L., Czerwiński, S., Daniau, A.-L., Dodson, J., Edwards, K. J., Edwards, M. E., Feurdean, A., Foster, D., Gajewski, K., Gałka, M., Garneau, M., Giesecke, T., Gil Romera, G., Girardin, M. P., Hoefer, D., Huang, K., Inoue, J., Jamrichová, E., Jasiunas, N., Jiang, W., Jiménez-Moreno, G., Karpińska-Kołaczek, M., Kołaczek, P., Kuosmanen, N., Lamentowicz, M., Lavoie, M., Li, F., Li, J., Lisitsyna, O., López-Sáez, J. A., Luelmo-Lautenschlaeger, R., Magnan, G., Magyari, E. K., Maksims, A., Marcisz, K., Marinova, E., Marlon, J., Mensing, S., Miroslaw-Grabowska, J., Oswald, W., Pérez-Díaz, S., Pérez-Obiol, R., Piilo, S., Poska, A., Qin, X., Remy, C. C., Richard, P. J. H., Salonen, S., Sasaki, N., Schneider, H., Shotyk, W., Stancikaite, M., Šteinberga, D., Stivrins, N., Takahara, H., Tan, Z., Trasune, L., Umbanhowar, C. E., Väliranta, M., Vassiljev, J., Xiao, X., Xu, Q., Xu, X., Zawisza, E., Zhao, Y., Zhou, Z., and Paillard, J.: The Reading Palaeofire Database: an expanded global resource to document changes in fire regimes from sedimentary charcoal records, Earth Syst. Sci. Data, 14, 1109–1124, https://doi.org/10.5194/essd-14-1109-2022, 2022.

Hochreiter, S. and Schmidhuber, J.: Long Short-Term Memory, Neural Comput., 9, 1735–1780, https://doi.org/10.1162/neco.1997.9.8.1735, 1997.

Hudiburg, T., Mathias, J., Bartowitz, K., Berardi, D. M., Bryant, K., Graham, E., Kolden, C. A., Betts, R. A., and Lynch, L.: Terrestrial carbon dynamics in an era of increasing wildfire, Nat. Clim. Change, 13, 1306–1316, https://doi.org/10.1038/s41558-023-01881-4, 2023.

Jain, P., Coogan, S. C. P., Subramanian, S. G., Crowley, M., Taylor, S., and Flannigan, M. D.: A review of machine learning applications in wildfire science and management, Environ. Rev., 28, 478–505, https://doi.org/10.1139/er-2020-0019, 2020.

Javier Gonzalez, A. S., Damianou, A., Paleyes, A., Winkelmolen, F., Shen, H., Hensman, J., Massiah, J., Fass, J., Lawrence, N., Berg Palm, R., Jenatton, R., Kamronn, S., and Dai, Z.: GPyOpt: A Bayesian Optimization framework in Python, GitHub [code], https://github.com/SheffieldML/GPyOpt (last access: 25 October 2024), 2016.

Jekel, C. F. and Venter, G.: pwlf: A Python Library for Fitting 1D Continuous Piecewise Linear Functions, GitHub [code], https://github.com/cjekel/piecewise_linear_fit_py (last access: 25 October 2024), 2019.

Jones, M. W., Abatzoglou, J. T., Veraverbeke, S., Andela, N., Lasslop, G., Forkel, M., Smith, A. J. P., Burton, C., Betts, R. A., van der Werf, G. R., Sitch, S., Canadell, J. G., Santín, C., Kolden, C., Doerr, S. H., and Le Quéré, C.: Global and Regional Trends and Drivers of Fire Under Climate Change, Rev. Geophys., 60, e2020RG000726, https://doi.org/10.1029/2020RG000726, 2022.

Joshi, J. and Sukumar, R.: Improving prediction and assessment of global fires using multilayer neural networks, Sci. Rep., 11, 3295, https://doi.org/10.1038/s41598-021-81233-4, 2021.

Kaplan, J. O. and Lau, K. H.-K.: The WGLC global gridded lightning climatology and time series, Earth Syst. Sci. Data, 13, 3219–3237, https://doi.org/10.5194/essd-13-3219-2021, 2021.

Klein Goldewijk, K., Beusen, A., Doelman, J., and Stehfest, E.: Anthropogenic land use estimates for the Holocene – HYDE 3.2, Earth Syst. Sci. Data, 9, 927–953, https://doi.org/10.5194/essd-9-927-2017, 2017.

Kobayashi, S., Ota, Y., Harada, Y., Ebita, A., Moriya, M., Onoda, H., Onogi, K., Kamahori, H., Kobayashi, C., Endo, H., Miyaoka, K., and Takahashi, K.: The JRA-55 Reanalysis: General Specifications and Basic Characteristics, J. Meteorol. Soc. Jpn. Ser. II, 93, 5–48, https://doi.org/10.2151/jmsj.2015-001, 2015.

Kreider, M. R., Higuera, P. E., Parks, S. A., Rice, W. L., White, N., and Larson, A. J.: Fire suppression makes wildfires more severe and accentuates impacts of climate change and fuel accumulation, Nat. Commun., 15, 2412, https://doi.org/10.1038/s41467-024-46702-0, 2024.

Kummu, M., Taka, M., and Guillaume, J. H. A.: Gridded global datasets for Gross Domestic Product and Human Development Index over 1990–2015, Sci. Data, 5, 180004, https://doi.org/10.1038/sdata.2018.4, 2018.

Lannom, K. O., Tinkham, W. T., Smith, A. M. S., Abatzoglou, J., Newingham, B. A., Hall, T. E., Morgan, P., Strand, E. K., Paveglio, T. B., Anderson, J. W., and Sparks, A. M.: Defining extreme wildland fires using geospatial and ancillary metrics, Int. J. Wildland Fire, 23, 322–337, 2014.

Lasslop, G., Brovkin, V., Reick, C. H., Bathiany, S., and Kloster, S.: Multiple stable states of tree cover in a global land surface model due to a fire-vegetation feedback, Geophys. Res. Lett., 43, 6324–6331, https://doi.org/10.1002/2016GL069365, 2016.

Li, F., Zhu, Q., Riley, W. J., Zhao, L., Xu, L., Yuan, K., Chen, M., Wu, H., Gui, Z., Gong, J., and Randerson, J. T.: AttentionFire_v1.0: interpretable machine learning fire model for burned-area predictions over tropics, Geosci. Model Dev., 16, 869–884, https://doi.org/10.5194/gmd-16-869-2023, 2023.

Li, W., MacBean, N., Ciais, P., Defourny, P., Lamarche, C., Bontemps, S., Houghton, R. A., and Peng, S.: Gross and net land cover changes in the main plant functional types derived from the annual ESA CCI land cover maps (1992–2015), Earth Syst. Sci. Data, 10, 219–234, https://doi.org/10.5194/essd-10-219-2018, 2018.

Libonati, R.: Megafires are here to stay – and blaming only climate change won't help, Nature, 627, 10, https://doi.org/10.1038/d41586-024-00641-4, 2024.

Lizundia-Loiola, J., Otón, G., Ramo, R., and Chuvieco, E.: A spatio-temporal active-fire clustering approach for global burned area mapping at 250 m from MODIS data, Remote Sens. Environ., 236, 111493, https://doi.org/10.1016/j.rse.2019.111493, 2020.

Long, T., Zhang, Z., He, G., Jiao, W., Tang, C., Wu, B., Zhang, X., Wang, G., and Yin, R.: 30 m Resolution Global Annual Burned Area Mapping Based on Landsat Images and Google Earth Engine, Global Annual Burned Area Maps (GABAM) [data set], https://doi.org/10.3390/rs11050489, 2019.

Lundberg, S. M., Erion, G., Chen, H., DeGrave, A., Prutkin, J. M., Nair, B., Katz, R., Himmelfarb, J., Bansal, N., and Lee, S.-I.: From local explanations to global understanding with explainable AI for trees, Nature Machine Intelligence, 2, 56–67, https://doi.org/10.1038/s42256-019-0138-9, 2020.

Luo, K., Wang, X., de Jong, M., and Flannigan, M.: Drought triggers and sustains overnight fires in North America, Nature, 627, 321–327, https://doi.org/10.1038/s41586-024-07028-5, 2024.

Meijer, J. R., Huijbregts, M. A. J., Schotten, K. C. G. J., and Schipper, A. M.: Global patterns of current and future road infrastructure, Environ. Res. Lett., 13, 064006, https://doi.org/10.1088/1748-9326/aabd42, 2018.

Meinshausen, N.: Quantile Regression Forests, J. Mach. Learn. Res., 7, 983–999, 2006.

Mouillot, F. and Field, C. B.: Fire history and the global carbon budget: a 1° × 1° fire history reconstruction for the 20th century, Glob. Change Biol., 11, 398-420, https://doi.org/10.1111/j.1365-2486.2005.00920.x, 2005.

Mouillot, F., Schultz, M. G., Yue, C., Cadule, P., Tansey, K., Ciais, P., and Chuvieco, E.: Ten years of global burned area products from spaceborne remote sensing – A review: Analysis of user needs and recommendations for future developments, Int. J. Appl. Earth Obs., 26, 64–79, https://doi.org/10.1016/j.jag.2013.05.014, 2014.

Nearing, G., Cohen, D., Dube, V., Gauch, M., Gilon, O., Harrigan, S., Hassidim, A., Klotz, D., Kratzert, F., Metzger, A., Nevo, S., Pappenberger, F., Prudhomme, C., Shalev, G., Shenzis, S., Tekalign, T. Y., Weitzner, D., and Matias, Y.: Global prediction of extreme floods in ungauged watersheds, Nature, 627, 559–563, https://doi.org/10.1038/s41586-024-07145-1, 2024.

Otón, G., Lizundia-Loiola, J., Pettinari, M. L., and Chuvieco, E.: Development of a consistent global long-term burned area product (1982–2018) based on AVHRR-LTDR data, Int. J. Appl. Earth Obs., 103, 102473, https://doi.org/10.1016/j.jag.2021.102473, 2021.

Page, S. E., Rieley, J. O., and Banks, C. J.: Global and regional importance of the tropical peatland carbon pool, Glob. Change Biol., 17, 798–818, https://doi.org/10.1111/j.1365-2486.2010.02279.x, 2011.

Paszke, A., Gross, S., Massa, F., Lerer, A., Bradbury, J., Chanan, G., Killeen, T., Lin, Z., Gimelshein, N., Antiga, L., Desmaison, A., Köpf, A., Yang, E., DeVito, Z., Raison, M., Tejani, A., Chilamkurthy, S., Steiner, B., Fang, L., Bai, J., and Chintala, S.: PyTorch: an imperative style, high-performance deep learning library, in: Proceedings of the 33rd International Conference on Neural Information Processing Systems, Vancouver, Canada, 8–14 December 2019, Curran Associates Inc., Article 721, 2019.

Pedregosa, F., Varoquaux, G., Gramfort, A., Michel, V., Thirion, B., Grisel, O., Blondel, M., Prettenhofer, P., Weiss, R., Dubourg, V., Vanderplas, J., Passos, A., Cournapeau, D., Brucher, M., Perrot, M., and Duchesnay, É.: Scikit-learn: Machine Learning in Python, J. Mach. Learn. Res., 12, 2825–2830, 2011.

Peng, S., Ciais, P., Maignan, F., Li, W., Chang, J., Wang, T., and Yue, C.: Sensitivity of land use change emission estimates to historical land use and land cover mapping, Global Biogeochem. Cy., 31, 626–643, https://doi.org/10.1002/2015GB005360, 2017.

Pessôa, A. C. M., Anderson, L. O., Carvalho, N. S., Campanharo, W. A., Junior, C. H. L. S., Rosan, T. M., Reis, J. B. C., Pereira, F. R. S., Assis, M., Jacon, A. D., Ometto, J. P., Shimabukuro, Y. E., Silva, C. V. J., Pontes-Lopes, A., Morello, T. F., and Aragão, L. E. O. C.: Intercomparison of Burned Area Products and Its Implication for Carbon Emission Estimations in the Amazon, Remote Sensing, 12, 3864, 2020.

Potapov, P., Turubanova, S., Hansen, M. C., Tyukavina, A., Zalles, V., Khan, A., Song, X.-P., Pickens, A., Shen, Q., and Cortez, J.: Global maps of cropland extent and change show accelerated cropland expansion in the twenty-first century, Nature Food, 3, 19–28, https://doi.org/10.1038/s43016-021-00429-z, 2022.

Power, M. J., Marlon, J. R., Bartlein, P. J., and Harrison, S. P.: Fire history and the Global Charcoal Database: A new tool for hy-

pothesis testing and data exploration, Palaeogeogr. Palaeoclim., 291, 52–59, https://doi.org/10.1016/j.palaeo.2009.09.014, 2010.

R Core Team: R: A language and environment for statistical computing, R Foundation for Statistical Computing, https://www.R-project.org/ (last access: 1 February 2024), 2024.

Randerson, J. T., Liu, H., Flanner, M. G., Chambers, S. D., Jin, Y., Hess, P. G., Pfister, G., Mack, M. C., Treseder, K. K., Welp, L. R., Chapin, F. S., Harden, J. W., Goulden, M. L., Lyons, E., Neff, J. C., Schuur, E. A. G., and Zender, C. S.: The Impact of Boreal Forest Fire on Climate Warming, Science, 314, 1130–1132, https://doi.org/10.1126/science.1132075, 2006.

Ribeiro, R. P. and Moniz, N.: Imbalanced regression and extreme value prediction, Mach. Learn., 109, 1803–1835, https://doi.org/10.1007/s10994-020-05900-9, 2020.

Rosan, T. M., Sitch, S., Mercado, L. M., Heinrich, V., Friedling-stein, P., and Aragão, L. E. O. C.: Fragmentation-Driven Divergent Trends in Burned Area in Amazonia and Cerrado, Frontiers in Forests and Global Change, 5, 801408, https://doi.org/10.3389/ffgc.2022.801408, 2022.

Santoro, M., Cartus, O., Carvalhais, N., Rozendaal, D. M. A., Avitabile, V., Araza, A., de Bruin, S., Herold, M., Quegan, S., Rodríguez-Veiga, P., Balzter, H., Carreiras, J., Schepaschenko, D., Korets, M., Shimada, M., Itoh, T., Moreno Martínez, Á., Cavlovic, J., Cazzolla Gatti, R., da Conceição Bispo, P., Dewnath, N., Labrière, N., Liang, J., Lindsell, J., Mitchard, E. T. A., Morel, A., Pacheco Pascagaza, A. M., Ryan, C. M., Slik, F., Vaglio Laurin, G., Verbeeck, H., Wijaya, A., and Willcock, S.: The global forest above-ground biomass pool for 2010 estimated from high-resolution satellite observations, Earth Syst. Sci. Data, 13, 3927–3950, https://doi.org/10.5194/essd-13-3927-2021, 2021.

Schoennagel, T., Balch, J. K., Brenkert-Smith, H., Dennison, P. E., Harvey, B. J., Krawchuk, M. A., Mietkiewicz, N., Morgan, P., Moritz, M. A., Rasker, R., Turner, M. G., and Whitlock, C.: Adapt to more wildfire in western North American forests as climate changes, P. Natl. Acad. Sci., 114, 4582–4590, https://doi.org/10.1073/pnas.1617464114, 2017.

Senande-Rivera, M., Insua-Costa, D., and Miguez-Macho, G.: Spatial and temporal expansion of global wildland fire activity in response to climate change, Nat. Commun., 13, 1208, https://doi.org/10.1038/s41467-022-28835-2, 2022.

Silva Junior, C. H. L., Aragão, L. E. O. C., Fonseca, M. G., Almeida, C. T., Vedovato, L. B., and Anderson, L. O.: Deforestation-Induced Fragmentation Increases Forest Fire Occurrence in Central Brazilian Amazonia, Forests, 9, 305, https://doi.org/10.3390/f9060305, 2018.

Sitch, S., Friedlingstein, P., Gruber, N., Jones, S. D., Murray-Tortarolo, G., Ahlström, A., Doney, S. C., Graven, H., Heinze, C., Huntingford, C., Levis, S., Levy, P. E., Lomas, M., Poulter, B., Viovy, N., Zaehle, S., Zeng, N., Arneth, A., Bonan, G., Bopp, L., Canadell, J. G., Chevallier, F., Ciais, P., Ellis, R., Gloor, M., Peylin, P., Piao, S. L., Le Quéré, C., Smith, B., Zhu, Z., and Myneni, R.: Recent trends and drivers of regional sources and sinks of carbon dioxide, Biogeosciences, 12, 653–679, https://doi.org/10.5194/bg-12-653-2015, 2015.

Sitch, S., O'Sullivan, M., Robertson, E., Friedlingstein, P., Albergel, C., Anthoni, P., Arneth, A., Arora, V. K., Bastos, A., Bastrikov, V., Bellouin, N., Canadell, J. G., Chini, L., Ciais, P., Falk, S., Harris, I., Hurtt, G., Ito, A., Jain, A. K., Jones,

M. W., Joos, F., Kato, E., Kennedy, D., Klein Goldewijk, K., Kluzek, E., Knauer, J., Lawrence, P. J., Lombardozzi, D., Melton, J. R., Nabel, J. E. M. S., Pan, N., Peylin, P., Pongratz, J., Poulter, B., Rosan, T. M., Sun, Q., Tian, H., Walker, A. P., Weber, U., Yuan, W., Yue, X., and Zaehle, S.: Trends and Drivers of Terrestrial Sources and Sinks of Carbon Dioxide: An Overview of the TRENDY Project, Global Biogeochem. Cy., 38, e2024GB008102, https://doi.org/10.1029/2024GB008102, 2024.

Song, X.-P., Hansen, M. C., Stehman, S. V., Potapov, P. V., Tyukavina, A., Vermote, E. F., and Townshend, J. R.: Global land change from 1982 to 2016, Nature, 560, 639–643, https://doi.org/10.1038/s41586-018-0411-9, 2018.

Tin Kam, H.: Random decision forests, Proceedings of 3rd International Conference on Document Analysis and Recognition, Montreal, QC, Canada, 14–16 August 1995, IEEE, vol. 271, 278–282, https://doi.org/10.1109/ICDAR.1995.598994, 1995.

Vancutsem, C., Achard, F., Pekel, J. F., Vieilledent, G., Carboni, S., Simonetti, D., Gallego, J., Aragão, L. E. O. C., and Nasi, R.: Long-term (1990–2019) monitoring of forest cover changes in the humid tropics, Sci. Adv., 7, eabe1603, https://doi.org/10.1126/sciadv.abe1603, 2021.

van der Werf, G. R., Randerson, J. T., Giglio, L., Collatz, G. J., Mu, M., Kasibhatla, P. S., Morton, D. C., DeFries, R. S., Jin, Y., and van Leeuwen, T. T.: Global fire emissions and the contribution of deforestation, savanna, forest, agricultural, and peat fires (1997–2009), Atmos. Chem. Phys., 10, 11707–11735, https://doi.org/10.5194/acp-10-11707-2010, 2010.

van der Werf, G. R., Randerson, J. T., Giglio, L., van Leeuwen, T. T., Chen, Y., Rogers, B. M., Mu, M., van Marle, M. J. E., Morton, D. C., Collatz, G. J., Yokelson, R. J., and Kasibhatla, P. S.: Global fire emissions estimates during 1997–2016, Earth Syst. Sci. Data, 9, 697–720, https://doi.org/10.5194/essd-9-697-2017, 2017.

Wagner, C. E. V.: Development and structure of the Canadian Forest Fire Weather Index System. Canadian Forestry Service, Headquarters, Ottawa, Forestry Technical Report 35, 35 pp., https://ostrnrcan-dostrncan.canada.ca/handle/1845/228434 (last access: 21 October 2023), 1987.

Wang, X., Wotton, B. M., Cantin, A. S., Parisien, M.-A., Anderson, K., Moore, B., and Flannigan, M. D.: cffdrs: an R package for the Canadian Forest Fire Danger Rating System, Ecol. Process., 6, 5, https://doi.org/10.1186/s13717-017-0070-z, 2017.

Yue, C., Ciais, P., Houghton, R. A., and Nassikas, A. A.: Contribution of land use to the interannual variability of the land carbon cycle, Nat. Commun., 11, 3170, https://doi.org/10.1038/s41467-020-16953-8, 2020.

Zhu, Q., Li, F., Riley, W. J., Xu, L., Zhao, L., Yuan, K., Wu, H., Gong, J., and Randerson, J.: Building a machine learning surrogate model for wildfire activities within a global Earth system model, Geosci. Model Dev., 15, 1899–1911, https://doi.org/10.5194/gmd-15-1899-2022, 2022.